A three-dimensional modal discontinuous Galerkin method for the second-order Boltzmann-Curtiss-based constitutive model of rarefied and microscale gas flows

S. Singh[a)], A. Karchani[1,b)], T. Chourushi[c)], and R. S. Myong[2,c)]

[a)]School of Physical and Mathematical Sciences, Nanyang Technological University, 21 Nanyang Link 637371, Singapore

[b)]ANSYS Inc., Lebanon, NH, US

[c)]School of Mechanical and Aerospace Engineering and ACTRC, Gyeongsang National University, Jinju, Gyeongnam 52828, South Korea

Abstract: A three-dimensional mixed modal discontinuous Galerkin (DG) method based on tetrahedral meshes was developed for simulating all flow regimes from subsonic to hypersonic rarefied and microscale gas flows within a single framework. The mixed modal DG scheme was used for solving conservation laws in conjunction with the second-order Boltzmann-Curtiss-based constitutive model of diatomic and polyatomic gases in strong thermal nonequilibrium. A decomposition algorithm based on the compression-expansion and velocity shear sub-problems was presented for solving the multi-dimensional second-order constitutive model. The Langmuir and Maxwell-Smoluchowski velocity-slip and temperature-jump boundary conditions were also implemented into the DG framework. To assess the ability of the new computational model to capture correct physical phenomena, we applied the new model to various gas flows in a wide range of continuum-rarefied and microscale regimes. The computational results in the rarefied and microscale flow regimes showed that the second-order

[1] Formerly research assistant at School of Mechanical and Aerospace Engineering, Gyeongsang National University, Jinju, South Korea.
[2] Corresponding author: Tel: +82-55-772-1645.
Email: myong@gnu.ac.kr.

constitutive model yielded solutions that were in better agreement with the direct simulation Monte Carlo and experimental data than the first-order constitutive model.

Keywords: Discontinuous Galerkin; Boltzmann-Curtiss-based constitutive model; Rarefied and microscale gas flows; Diatomic and polyatomic gases

1 Introduction

The flow and thermal physics of rarefied and microscale gases has remained a challenging topic in the field of physical and computational gas dynamics. Research in the field includes the development of theoretical and computational tools [1-7] to predict the flow and thermal physics of re-entry (or gliding) vehicles flying through layers of Earth's atmosphere at hypersonic speed, and for micro-electro-mechanical systems (MEMS). In these applications, thermal nonequilibrium phenomena associated with rarefaction and microscale gas–surface interactions occur [1], and viscous force and thermal transfer play important roles. The degree of rarefaction can be characterized by the Knudsen number, which is defined as the ratio of the molecular mean fee path to a characteristic physical length. The main source of thermal nonequilibrium is the insufficient number of collisions between particles in the high Knudsen number condition. Such thermal nonequilibria are linearly amplified at increasing Mach number. The theoretical and computational modelling of rarefied and microscale gas flows under strong thermal nonequilibrium conditions has therefore been very challenging [8-22].

Computational simulations are often employed to investigate the rarefied and microscale gas flows that arise in various applications. The two most prominently used strategies are computational fluid dynamics (CFD) methods, mostly based on the Navier-Stokes-Fourier (called NSF hereafter) equations [23], and the direct simulation Monte Carlo (DSMC) method [2]. In CFD methods, the NSF equations are used as the basic tenet for computational modelling. The basic form of the NSF equations was derived in 1822, and these two-century old equations of fluid dynamics are accepted as the *de-facto* mathematical models for every possible flow problem. However, there are caveats associated with this otherwise complete model.

A vital assumption, the so-called Stokes' hypothesis, was introduced in the derivation of the NSF relations by Stokes [24] in 1845, in which bulk (or volume) viscosity μ_b vanishes (λ and μ being the second coefficient of viscosity and the shear viscosity of the fluid, respectively),

$$\mu_b \equiv \lambda + \frac{2}{3}\mu = 0, \quad \text{equivalently } \lambda = -\frac{2}{3}\mu. \tag{1.1}$$

In the Stokes' hypothesis, it is assumed that the dilatational term $\nabla \cdot \mathbf{u}$ does not play any role in the level of the constitutive equation of viscous stress, even though it may play a significant role in the level of conservation laws, like shock-dominated compressible gas flows. While the Stokes' hypothesis is certainly legitimate for monatomic gases like argon, there is ever increasing evidence that now indicates this is not the case for diatomic and polyatomic gases—like nitrogen (or air), hydrogen, methane, and carbon dioxide [25-41]. Examples of such cases include the viscous inner structure of shock waves in diatomic and polyatomic gases, and hypersonic entry into the Mars atmosphere, which consists mostly of carbon dioxide.

Indeed, in contrast to the Stokes' hypothesis, a recent experimental study on the instability in the laminar-to-turbulence transition in hypersonic boundary layers showed that, for a real diatomic gas, the growth and decay of the second mode in instability is accompanied by a dilatation process, which leads to a significant increase in dilatation dissipation, by as much as 50% [29]. Moreover, direct numerical simulation (DNS) studies of compressible turbulence have shown that bulk viscosity significantly increases the decay rate of turbulent kinetic energy, and dilatation is reduced by over two orders of magnitude within the first two eddy-turnover times [30]. Furthermore, a significant increment in enstrophy was observed with increasing bulk viscosity, which is directly related to the rotational mode of gas molecules [33].

In a recent study [34], it was shown that in diatomic and polyatomic gases the bulk viscosity ratio plays an essential role in determining the type of topology of the constitutive models. With increasing bulk viscosity ratio, the topology changes from an ellipse to a circle, to a parabola, and then finally to a hyperbola, just like the orbits of planets and comets in the two-body Kepler problem. The ultimate

origin of the rich topology of various conic sections was traced to the bulk viscosity ratio, and its subtle interplay with the tight coupling of the viscous stress and the velocity gradient of a kinematic nature in strong thermal nonequilibrium.

Another vital assumption introduced in the derivation of the NSF relations is near the local-thermal-equilibrium (LTE), and as a result, their validity may be seriously questioned in flows whose status is not near the LTE conditions, like rarefied and microscale gases. The classical description based on the first-order linear NSF constitutive laws is known to suffer from serious limitations when predicting the correct flow behaviour of diatomic and polyatomic gases in strong thermal nonequilibrium states. Simple modification of transport coefficients in the classical NSF theory, or the introduction of velocity-slip and temperature-jump boundary conditions alone, cannot solve the current problems in the study of diatomic and polyatomic gas flows in strong thermal nonequilibrium. Consequently, high-order constitutive equations beyond the first-order level need to be derived from proper master kinetic equations for diatomic and polyatomic gases.

On the other hand, there is another prominent strategy readily available for investigating rarefied and microscale gas flows. The direct simulation Monte Carlo (DSMC) method [2] is considered the most powerful strategy for simulating rarefied gas flows. In sharp contrast to the CFD methods, based on the conservation laws, the DSMC is not based on any partial differential equations, but is rather a pure computational method that directly simulates the motion of gases through probabilistic collision models.

Other approximation or solution methods for studying rarefied and microscale gases have also been developed, such as the Boltzmann model equations [42-44], Wang-Chang-Uhlenbeck model [45], Fokker-Planck based kinetic model [46], and Rykov model [47]. However, except for Wu *et al*.' model [44], these kinetic models suffer a common drawback in the study of diatomic and polyatomic gases that they do not reduce to the original Boltzmann equation for monatomic gases when a translational–internal energy exchange is absent. In addition, various other kinetic schemes have been proposed, including the discrete velocity method [48], unified gas-kinetic scheme [49], discrete unified gas-kinetic scheme [50], and gas-kinetic unified algorithm [51]. Recently, a novel solver based on a combination

of kinetic flux solver, discrete velocity method and moment method was developed to simulate flows from continuum to rarefied regimes at moderate Knudsen number [52].

Independently of the aforementioned methods, Myong [8-13] developed a distinct approach for rarefied and microscale gases, based on the second-order constitutive relation beyond the conventional first-order accuracy. The second-order constitutive relations for diatomic and polyatomic gases were systematically derived from the Boltzmann-Curtiss kinetic equation [53-55] based on Eu's modified moment method [6,7] and Myong's closing-last balanced closure [56]. The Boltzmann-Curtiss kinetic equation additionally introduces the angular momentum and azimuth angle associated with the rotational mode of molecules to the kinetic formulation, and smoothly extends the original Boltzmann kinetic equation to diatomic and (linear) polyatomic gases. An important result obtained in these studies is that constitutive relations between stresses (and heat flux) and the strain rate (and the temperature gradient) are generally nonlinear and coupled in states far from thermal equilibrium. The second-order constitutive model has been successfully applied to some challenging problems of non-equilibrium gas flows where the first-order Navier-Stokes-Fourier (NSF) with Stokes' hypothesis (1.1) and Navier-Fourier (NF) relations were found to be inappropriate [8-21, 32-34, 56-59]. The second-order constitutive model has also been validated for the velocity-shear dominated force-driven Poiseuille gas flow using deterministic atomic-level microscopic molecular dynamics (MD) [60].

Discontinuous Galerkin (DG) methods are being increasingly studied as a computational tool to solve various partial differential equations that arise in diverse scientific and engineering problems. The DG method was initially developed by Reed and Hill [61] for solving the neutron transport problem, based on a high order finite element discretization. Various researchers [62-66] further contributed to develop the DG methods for convection-diffusion systems. The DG methods are built on a hybridization of the finite volume and finite element methods, which incorporates the main properties commonly associated with these two methods. The DG methods have numerous features, including robustness with strong mathematical properties, and are well defined for the structured and unstructured meshes associated within complex geometries. They are well suited for non-conforming elements having hanging nodes; are very efficient for adopting time-stepping algorithms and *hp* adaptivity; and highly

parallelizable. Recently, the DG methods have also been used to design deterministic solvers for kinetic equations such as multi-scale kinetic flow problems [67,68], plasma physics problems [69,70] and Boltzmann based quantum physics problems [71-73].

The aim of the present work is to develop a three-dimensional mixed modal discontinuous Galerkin method for solving conservation laws in conjunction with the second-order Boltzmann–Curtiss-based constitutive model for rarefied and microscale gas flows. The main emphasis is placed on how to solve the second-order constitutive model arising from the high degree of thermal nonequilibrium in multi-dimensional gas flow situations within the Galerkin framework. We focus on developing a three-dimensional modal DG method based on tetrahedral meshes for the second-order constitutive model of diatomic and polyatomic gases in rarefied and microscale flow regimes.

There is another feature in the proposed DG method: In contrast to the conventional finite volume formulation, in which only the boundary surface integral is required, the volume integral is additionally required in the DG formulation. To solve the multi-dimensional second-order constitutive model in conjunction with the multi-dimensional conservation laws, the present study develops a decomposition algorithm of compression-expansion and velocity-shear flows that can handle not only the boundary surface integral but also the volume integral.

For the verification and validation study, we apply the new methods to various gas flows in a wide range of continuum-rarefied and microscale regimes. Examples of such problems include the viscous inner structure of one-dimensional shock waves for all Mach numbers, two-dimensional subsonic and hypersonic flows past a cylinder, two-dimensional internal rarefied and microscale cylindrical Couette flow with a moving wall, three-dimensional subsonic and hypersonic flows past a sphere, three-dimensional hypersonic flows over a flat plate, and a hypersonic flow around a suborbital IXV re-entry vehicle.

The present paper is organized as follows. In Section 2, we consider the Boltzmann-Curtiss kinetic equation of diatomic and polyatomic gases and derive the second-order constitutive equations for non-conserved variables, as well as the conservation laws for conserved variables. Two fundamental sub-problems related to the second-order constitutive equations—compression-expansion and velocity-

shear—and their extension to the volume integral in three-dimensional formulation are also presented. In Section 3, a three-dimensional mixed modal discontinuous Galerkin is developed. The positivity preserving limiter for tetrahedral elements is developed for the present DG scheme. The Maxwell velocity slip and Smoluchowski temperature jump boundary conditions, which are essential in any efficient computational simulation of rarefied microscale gas flows, are implemented for the gas-surface molecular interaction in the DG framework. In Section 4, we investigate various flows of rarefied and microscale gases in a wide range of continuum-rarefied and microscale regimes. We then present numerical results of the multi-dimensional flow problems to demonstrate the feasibility of the computational models and to validate the accuracy of the numerical scheme. Finally, in Section 5, we provide some concluding remarks and discuss issues of further development in line with the present study.

2 Second-order constitutive model of diatomic and polyatomic gases: complexity out of simplicity and decomposed computation

2.1 The Boltzmann-Curtiss kinetic equation of diatomic and polyatomic gases and the exact conservation laws

When there is no external force field, the Boltzmann-Curtiss kinetic equation for diatomic (and linear polyatomic) molecules with a moment of inertia I_m and an angular momentum **j** can be expressed [54] as follows,

$$\left(\frac{\partial}{\partial t} + \mathbf{v} \cdot \nabla + \frac{j}{I_m} \frac{\partial}{\partial \psi} \right) f\left(\mathbf{v}, \mathbf{r}, \mathbf{j}, \psi, t\right) = R\left[f \right]. \tag{2.1}$$

Here, $f, \mathbf{v}, \mathbf{r}, \psi, j$ and $R\left[f \right]$ represent the distribution function of the population of molecules, the velocity, the particle position, the azimuthal angle associated with the orientation of the molecules, the magnitude of the angular momentum vector **j**, and the collision integral, respectively. When we ignore the angular momentum of the molecule related to the rotational mode, the Boltzmann-Curtiss kinetic equation recovers the original Boltzmann kinetic equation for a monatomic gas

$$\left(\frac{\partial}{\partial t}+\mathbf{v}\cdot\nabla\right)f\left(\mathbf{v},\mathbf{r},t\right)=C\left[f\right],$$

where $C\left[f\right]$ represents the Boltzmann collision integral of the interaction between two particles. The macroscopic quantities, conserved variables $\left(\rho,\rho\mathbf{u},\rho E\right)$ and the non-conserved variables $\left(\mathbf{\Pi},\Delta,\mathbf{Q}\right)$, can be defined using the following statistical relationships:

$$\phi^{(h)}=\left\langle h^{(k)}f\right\rangle, \tag{2.2}$$

where the angular bracket denotes the integration of microscopic variables $\mathbf{v},\mathbf{j},\psi$ in the computational domain. The $h^{(k)}$ indicates the molecular expressions of the *h*-th moments of the distribution function and $\phi^{(h)}$ denotes the equivalent macroscopic quantity. The leading elements of the macroscopic set of the conserved and non-conserved variables are defined as [53],

$$\begin{aligned}&\phi^{(1)}=\rho,\ \phi^{(2)}=\rho\mathbf{u},\ \phi^{(3)}=\rho E,\\&\phi^{(4)}=\mathbf{\Pi}=\left[\mathbf{P}\right]^{(2)},\ \phi^{(5)}=\Delta=\frac{1}{3}\text{Trace}\,\mathbf{P}-p,\ \phi^{(6)}=\mathbf{Q},\end{aligned} \tag{2.3}$$

where **u** is the velocity vector, *E* is the total energy density, while $\mathbf{\Pi},\Delta,\mathbf{Q}$ represent the shear stress tensor, the excess normal stress, and the heat flux, respectively. And the corresponding molecular expressions to this set read as

$$\begin{aligned}&h^{(1)}=m,\ h^{(2)}=m\mathbf{v},\ h^{(3)}=\frac{1}{2}mC^2+H_{rot},\\&h^{(4)}=\left[m\mathbf{C}\mathbf{C}\right]^{(2)},\ h^{(5)}=\frac{1}{3}mC^2-p/n,\ h^{(6)}=\left(\frac{1}{2}mC^2+H_{rot}-m\hat{h}\right)\mathbf{C},\end{aligned} \tag{2.4}$$

where *m* is the molecular mass, **C** = **v** – **u** is the peculiar velocity of the molecule, *n* is the number density per unit mass, $\hat{h}$ is the enthalpy density per unit mass, and $H_{rot}=j^2/2I_m$ is the rotational Hamiltonian of the particle.

The viscous stresses Π and Δ are related to the stress tensor **P** through the relation

$$\mathbf{P} = \left(p + \Delta \right)\mathbf{I} + \mathbf{\Pi}. \tag{2.5}$$

Here, **I** is the unit second rank tensor. The symbol $\left[\mathbf{A}\right]^{(2)}$ denotes the traceless symmetric part of the second-rank tensor **A**,

$$\left[\mathbf{A}\right]^{(2)} = \frac{1}{2}\left(\mathbf{A} + \mathbf{A}^{t}\right) - \frac{1}{3}\mathbf{I}\,\mathrm{Trace}\,\mathbf{A}. \tag{2.6}$$

The pressure p and temperature T are related through the equation of state $p = nk_B T = \rho RT$. Note that the excess normal stress Δ also contributes to the forces and moments exerting on the object, when integrating distributions of the pressure, shear stress tensor, and excess normal stress over the surface.

The conservation laws of mass, momentum, and total energy for diatomic and polyatomic gases can be derived directly from the Boltzmann-Curtiss kinetic equation by noting that the molecular expressions for conserved variables (2.4) are collision invariants, and thus there is no dissipation term appearing in the right-hand side of the balance equation, i.e. $\left\langle h^{(1,2,3)} R\left[f \right] \right\rangle = 0$. After differentiating the statistical definition of the conserved variables with time and combining them with the Boltzmann-Curtiss kinetic equation, the following conservation laws, all of which are an exact consequence of the Boltzmann-Curtiss kinetic equation, can be derived [10, 53],

$$\frac{\partial}{\partial t}\begin{bmatrix} \rho \\ \rho\mathbf{u} \\ \rho E \end{bmatrix} + \nabla\cdot\begin{bmatrix} \rho\mathbf{u} \\ \rho\mathbf{u}\mathbf{u} + p\mathbf{I} \\ \left(\rho E + p\right)\mathbf{u} \end{bmatrix} + \nabla\cdot\begin{bmatrix} 0 \\ \mathbf{\Pi} + \Delta\mathbf{I} \\ \left(\mathbf{\Pi} + \Delta\mathbf{I}\right)\cdot\mathbf{u} + \mathbf{Q} \end{bmatrix} = 0. \tag{2.7}$$

After the following dimensionless variables and parameters are introduced,

$$\begin{aligned} &t^* = \frac{t}{\left(L/u_r\right)},\ \ \boldsymbol{x}^* = \frac{\boldsymbol{x}}{L},\ \ \mu^* = \frac{\mu}{\mu_r},\ k^* = \frac{k}{k_r},\ \ \boldsymbol{u}^* = \frac{\boldsymbol{u}}{u_r},\ \ p^* = \frac{p}{p_r},\ \ \rho^* = \frac{\rho}{\rho_r}, \\ &T^* = \frac{T}{T_r},\ \ C_p^* = \frac{C_p}{C_{pr}},\ \ E^* = \frac{E}{u_r^2},\ \ \mathbf{\Pi}^* = \frac{\mathbf{\Pi}}{\left(\mu_r u_r/L\right)},\ \ \Delta^* = \frac{\Delta}{\left(\mu_{b_r} u_r/L\right)},\ \ \mathbf{Q}^* = \frac{\mathbf{Q}}{\left(k_r \Delta T/L\right)}, \end{aligned} \tag{2.8}$$

where the subscript *r* stands for the reference state, *L* denotes the characteristic length, C_p denotes the heat capacity per mass at constant pressure, k is the Chapman-Enskog thermal conductivity. The non-dimensional conservation laws for diatomic and polyatomic gases (with the asterisks omitted for notational brevity) can be written as [10],

$$\frac{\partial \mathbf{U}}{\partial t} + \nabla \cdot \mathbf{F}^{\text{inv}}\left(\mathbf{U}\right) + \nabla \cdot \mathbf{F}^{\text{vis}}\left(\mathbf{U}, \boldsymbol{\Pi}, \Delta, \mathbf{Q}\right) = 0, \tag{2.9}$$

where the matrices and other variables are defined as

$$\mathbf{U} = \begin{bmatrix} \rho \\ \rho \mathbf{u} \\ \rho E \end{bmatrix}, \quad \mathbf{F}^{\text{inv}} = \begin{bmatrix} \rho \mathbf{u} \\ \rho \mathbf{u}\mathbf{u} + \dfrac{1}{\gamma M^2} p\mathbf{I} \\ \left(\rho E + \dfrac{1}{\gamma M^2} p\right)\mathbf{u} \end{bmatrix}, \quad \mathbf{F}^{\text{vis}} = \frac{1}{\text{Re}} \begin{bmatrix} 0 \\ \boldsymbol{\Pi} + f_b \Delta \mathbf{I} \\ \left(\boldsymbol{\Pi} + f_b \Delta \mathbf{I}\right) \cdot \mathbf{u} + \dfrac{1}{\text{Ec}\,\text{Pr}} \mathbf{Q} \end{bmatrix}. \tag{2.10}$$

Here the dimensionless parameters such as Mach number (*M*), Reynolds number (Re), Eckert number (Ec) and Prandtl number (Pr) can be defined as

$$M \equiv \frac{u_r}{\sqrt{\gamma R T_r}}, \ \text{Re} \equiv \frac{\rho_r u_r L}{\mu_r}, \ \text{Ec} \equiv \left(\gamma - 1\right) M^2, \ \text{Pr} \equiv \frac{c_{p_r} \mu_r}{k_r}, \ f_b = \frac{\mu_{b_r}}{\mu_r}. \tag{2.11}$$

The specific heat ratio γ is assumed to be 5/3 for argon gas, 7/5 for nitrogen gas, and 1.29 for carbon dioxide gas. The factor $f_b = \mu_{b_r} / \mu_r$ is the ratio of the bulk viscosity to the shear viscosity. Its value may be experimentally determined using a sound wave absorption measurement. The value of the Prandtl number (Pr) may be calculated through Eucken's relation

$$\text{Pr} = \frac{4\gamma}{9\gamma - 5}. \tag{2.12}$$

It is worth mentioning that the Eucken relationship (2.12) is obtained as a first-order approximation, and, recently, studies have been conducted to improve the accuracy by adding higher-order corrections [74] or tuning with experimental data [75].

2.2 Zeroth-order Boltzmann-Curtiss-based (Euler) constitutive model

The zeroth-order Boltzmann-Curtiss-based (Euler) constitutive model is a direct consequence of assuming flow in an equilibrium state, that is, the Maxwellian distribution function [6]. Therefore, the zeroth-order Boltzmann-Curtiss-based constitutive model of the shear stress, the excess normal stress, and the heat flux vector is reduced to the following relations

$$\boldsymbol{\Pi} = 0, \;\; \Delta = 0, \;\; \mathbf{Q} = 0. \tag{2.13}$$

Applying these constitutive relationships into the exact conservation laws (2.7) will result in the well-known Euler system of equations.

2.3. First-order Boltzmann-Curtiss-based (Navier-Fourier) constitutive model

After differentiating the statistical definition of the non-conserved variables $h^{(4,5,6)}$ with time and combining them with the Boltzmann-Curtiss kinetic equation, the following first-order Boltzmann-Curtiss-based Navier-Stokes (NF) constitutive model of the shear stress tensor, the excess normal stress, and the heat flux vector can be obtained,

$$\boldsymbol{\Pi} = -2\mu\left[\nabla\mathbf{u}\right]^{(2)}, \;\; \Delta = -\mu_b \nabla\cdot\mathbf{u}, \;\; \mathbf{Q} = -k\nabla T. \tag{2.14}$$

During this process, the first-order balanced closure was applied [56].

Once the Stokes' hypothesis (1.1) is further applied, that means $\mu_b = 0$, the first-order NF constitutive equations (2.14) are reduced to the well-known linear NSF constitutive equations. It should be noted that these first-order linear relations were obtained after very crude approximations; all kinematic terms except for the thermodynamic force term were neglected in the moment equations and the collision-related dissipation terms $\left\langle h^{(4,5,6)} R\left[f \right] \right\rangle$ were linearized.

At this stage, it should be mentioned that the bulk viscosity μ_b can also be viewed as a quantity directly related to the relaxation time associated with the rotational degrees of freedom. It can be shown that the excess normal stress Δ is equivalent to the difference between the translational and rotational temperatures [76]. Thus, the hydrodynamic equation can be formulated in two ways: either introducing the excess normal stress and keeping one temperature concept or introducing two temperatures but no excess normal stress. The former was taken in the present study because it is a natural extension of the first-order Navier-Fourier constitutive model (2.14) and the one-temperature hydrodynamics is more natural to connect with the laws of thermodynamics.

In these expressions, the following Chapman-Enskog linear transport coefficients [76,77] can be employed

$$\mu = T^s, \mu_b = f_b \mu, k = T^s, \tag{2.15}$$

where *s* stands for the index of the inverse power laws of gas molecules, given as

$$s = \frac{1}{2} + \frac{2}{(\nu - 1)}. \tag{2.16}$$

Here, the parameter ν is the exponent of the inverse power laws for the gas-particle interaction potentials. The value of *s* was assumed to be 0.81 for argon gas, 0.78 for nitrogen, and 0.93 for carbon dioxide gas [77]. The values of the factor f_b appearing in the bulk viscosity (2.15) were considered to be 0.0, 0.8, and 1000, respectively, for argon, nitrogen, and carbon dioxide gases, based on experiments [78].

2.4 Second-order Boltzmann-Curtiss-based constitutive model

Similarly, we can derive the high-order constitutive model by first differentiating the statistical definition of the non-conserved variables $h^{(4,5,6)}$ with time and then combining them with the Boltzmann-Curtiss kinetic equation,

$$\rho\frac{D}{Dt}\left(\frac{\boldsymbol{\Pi}}{\rho}\right)+\nabla\cdot\boldsymbol{\Psi}^{(\Pi)}+2\left[\boldsymbol{\Pi}\cdot\nabla\mathbf{u}\right]^{(2)}+2\left(\Delta+p\right)\left[\nabla\mathbf{u}\right]^{(2)}=\left\langle h^{(4)}R\left[f\right]\right\rangle,$$
$$\rho\frac{D}{Dt}\left(\frac{\Delta}{\rho}\right)+\nabla\cdot\boldsymbol{\Psi}^{(\Delta)}+2\gamma'\left(\boldsymbol{\Pi}+\Delta\mathbf{I}\right):\nabla\mathbf{u}+\frac{2}{3}\gamma' p\nabla\cdot\mathbf{u}=\left\langle h^{(5)}R\left[f\right]\right\rangle, \tag{2.17}$$
$$\rho\frac{D}{Dt}\left(\frac{\mathbf{Q}}{\rho}\right)+\nabla\cdot\boldsymbol{\Psi}^{(\mathrm{Q})}+\boldsymbol{\Psi}^{(\mathrm{P})}:\nabla\mathbf{u}+\frac{D\mathbf{u}}{Dt}\cdot\boldsymbol{\Pi}+\mathbf{Q}\cdot\nabla\mathbf{u}+\left(\boldsymbol{\Pi}+\Delta\mathbf{I}+p\mathbf{I}\right)\cdot C_p\nabla T=\left\langle h^{(6)}R\left[f\right]\right\rangle.$$

Here, $\gamma'=\left(5-3\gamma\right)/2$ and $\boldsymbol{\Psi}^{(\Pi,\Delta,\mathrm{Q},\mathrm{P})}$ represent the open high-order terms of the shear stress, the excess normal stress, the heat flow, and the stress, respectively. At this point, it should be mentioned that the constitutive equations for the non-conserved variables (2.17) are an exact consequence of the Boltzmann-Curtiss kinetic equation (2.1) and are thus capable of capturing the whole flow physics, if they are provided with the accurate closure on the higher-order terms $\boldsymbol{\Psi}^{(\Pi,\Delta,\mathrm{Q},\mathrm{P})}$ and $\left\langle h^{(4,5,6)}R\left[f\right]\right\rangle$.

However, it turns out that the derivation of the second-order constitutive model is extremely difficult, mainly due to two fundamental issues: the so-called closure problem and accurate treatment of the dissipation terms $\left\langle h^{(4,5,6)}R\left[f\right]\right\rangle$, both of which have remained unsolved for several decades.

Myong in 2014 proposed a new closure theory [56], known as "closing-last balanced closure," from a keen observation of the essence of the closure problem in a complex system. When closing open terms in the moment equations derived from the kinetic equation, the number of places to be closed was found to be two (movement and interaction), rather than one (movement only), having been misled by the Maxwellian molecule assumption in the previous theory [4]. For example, there are two terms requiring closure in the constitutive equation of viscous stress in (2.17): $\nabla\cdot\boldsymbol{\Psi}^{(\Pi)}$ and $\left\langle h^{(4)}R\left[f\right]\right\rangle$. Therefore, the order of approximations in handling the two terms—kinematic (movement) and dissipation (interaction) terms—must be the same to satisfy balancing; for instance, the second-order for both terms. This achieves a balance between the kinematic and collision term approximation, namely, the second-order closure for the kinematic terms,

$$\nabla\cdot\boldsymbol{\Psi}^{(\Pi)}=\nabla\cdot\boldsymbol{\Psi}^{(\Delta)}=\nabla\cdot\boldsymbol{\Psi}^{(\mathrm{Q})}+\boldsymbol{\Psi}^{(\mathrm{P})}:\nabla\mathbf{u}=0,$$

while maintaining the same second-order closure for $\left\langle h^{(4,5,6)} R[f] \right\rangle$.

In this balanced closure theory, third-order closure for $\left\langle h^{(4)} R[f] \right\rangle$ in the constitutive equation of viscous stress may not be essential; in fact, unbalanced higher-order closure in the moment method may not provide improved solutions as promised, especially in the case of a high Mach number shock structure problem [56]. It should be mentioned that the present balanced closure effectively resolves the weakness of Eu's closure [6], like $\mathbf{\Psi}^{(\mathrm{p})} \left(\equiv \langle m\mathbf{CCC}f \rangle \right) = 0$, which was strongly criticised by mathematicians and physicists for its inconsistency, i.e., that the term $\langle m\mathbf{CCC}f \rangle$ cannot be zero in general, especially in strong thermal nonequilibrium.

On the other hand, to accurately calculate the dissipation terms while making the underlying theory compatible with the second law of thermodynamics, Eu in 1980 proposed a canonical distribution function in the exponential form, after recognizing the logarithmic form of the non-equilibrium entropy production [53]. Unlike Grad's Hermite polynomial expansion [4], the cumulant expansion of the distribution function in the series of the 1st-mean, 2nd-variance, 3rd-skewness, 4th-excess (or kurtosis), etc., assured the non-negativity of the distribution function regardless of the level of approximations [6,7,39,56].

When the balanced closure and cumulant expansion are applied to Eq. (2.17), it is reduced to

$$
\begin{aligned}
&\rho \frac{D}{Dt}\left(\frac{\mathbf{\Pi}}{\rho} \right) + 2\left[\mathbf{\Pi} \cdot \nabla \mathbf{u} \right]^{(2)} + 2\left(\Delta + p \right) \left[\nabla \mathbf{u} \right]^{(2)} = -\frac{p}{\mu} \mathbf{\Pi} q_{2\mathrm{nd}}(\kappa), \\
&\rho \frac{D}{Dt}\left(\frac{\Delta}{\rho} \right) + 2\gamma' \left(\mathbf{\Pi} + \Delta \mathbf{I} \right) : \nabla \mathbf{u} + \frac{2}{3} \gamma' p \nabla \cdot \mathbf{u} = -\frac{2}{3} \gamma' \frac{p}{\mu_b} \Delta q_{2\mathrm{nd}}(\kappa), \\
&\rho \frac{D}{Dt}\left(\frac{\mathbf{Q}}{\rho} \right) + \frac{D\mathbf{u}}{Dt} \cdot \mathbf{\Pi} + \mathbf{Q} \cdot \nabla \mathbf{u} + \left(\mathbf{\Pi} + \Delta \mathbf{I} + p\mathbf{I} \right) \cdot C_p \nabla T = -\frac{pC_p}{k} \mathbf{Q} q_{2\mathrm{nd}}(\kappa).
\end{aligned}
\tag{2.18}
$$

Here the exact form of the first-order cumulant expansion κ appearing on the right-hand side of the collision integrals can be calculated using the Chapman-Enskog theory [77]. The first-order reduced collision integral is expressed as a modified Rayleigh-Onsager dissipation function

$$q_{2\mathrm{nd}}(\kappa)=\frac{\sinh\kappa}{\kappa},\quad \kappa=\frac{(mk_B)^{1/4}}{\sqrt{2}d}\frac{T^{1/4}}{p}\left[\frac{\mathbf{\Pi}:\mathbf{\Pi}}{2\mu}+\gamma'\frac{\Delta^2}{\mu_b}+\frac{\mathbf{Q}\cdot\mathbf{Q}/T}{k}\right]^{1/2}.$$

Note that the transport coefficients in Eq. (2.18) are now second-order in the form of $(\mu,\mu_b,k)/q_{2\mathrm{nd}}(\kappa)$.

Furthermore, the temporal dependence in the equations can be neglected, owing to the very short relaxation times of the non-conserved variables, being on the order of 10^{-10} second [6,8], compared to those for conserved variables and the characteristic times of the flow process. This so-called adiabatic approximation simplifies the partial differential equation into a set of algebraic equations, which greatly reduces the numerical complexities involved in solving the constitutive equations.

Once these tenets—the aforementioned closing-last balanced closure, and Eu's cumulant expansion based on the canonical distribution function in the exponential form to the explicit calculation of the dissipation term—are applied to the constitutive equations (2.17) and after introducing the adiabatic approximation to (2.18), the following second-order constitutive model for diatomic and polyatomic gases [10] can be derived,

$$\begin{aligned}
&\left[\hat{\mathbf{\Pi}}\cdot\nabla\hat{\mathbf{u}}\right]^{(2)}+\left(1+f_b\hat{\Delta}\right)\hat{\mathbf{\Pi}}_0=\hat{\mathbf{\Pi}}q_{2\mathrm{nd}}(c\hat{R}),\\
&\frac{3}{2}\left(\hat{\mathbf{\Pi}}+f_b\hat{\Delta}\mathbf{I}\right):\nabla\hat{\mathbf{u}}+\hat{\Delta}_0=\hat{\Delta}q_{2\mathrm{nd}}(c\hat{R}),\\
&\hat{\mathbf{\Pi}}\cdot\hat{\mathbf{Q}}_0+\left(1+f_b\hat{\Delta}\right)\hat{\mathbf{Q}}_0=\hat{\mathbf{Q}}q_{2\mathrm{nd}}(c\hat{R}),
\end{aligned}\tag{2.19}$$

where

$$q_{2\mathrm{nd}}(c\hat{R})=\frac{\sinh(c\hat{R})}{c\hat{R}},\ \hat{R}=\frac{N_\delta}{p}\left[\hat{\mathbf{\Pi}}:\hat{\mathbf{\Pi}}+2\gamma' f_b\hat{\Delta}^2+\hat{\mathbf{Q}}\cdot\hat{\mathbf{Q}}\right]^{1/2}.$$

During the derivation, we also assumed that the effect of the term $\mathbf{Q}\cdot\nabla\mathbf{u}$ in the equation for the heat flux is negligible. All terms in equations (2.19) are normalized by introducing proper variables and parameters,

$$\hat{\boldsymbol{\Pi}} \equiv \frac{N_\delta}{p}\boldsymbol{\Pi},\ \hat{\Delta} \equiv \frac{N_\delta}{p}\Delta,\ \hat{\mathbf{Q}} \equiv \frac{N_\delta}{p}\frac{\mathbf{Q}}{\sqrt{T/(2\varepsilon)}},\ \nabla\hat{\mathbf{u}} \equiv -2\mu\frac{N_\delta}{p}\nabla\mathbf{u}, \tag{2.20}$$

$$N_\delta \equiv \frac{\mu_r u_r / L}{p_r} = \frac{\gamma M^2}{\mathrm{Re}} = \mathrm{Kn}\, M\sqrt{\frac{2\gamma}{\pi}},\ \varepsilon \equiv \frac{1}{Ec\,\mathrm{Pr}}.$$

Here the caret (^) over a symbol represents a quantity with the dimension of the ratio of the stress to the pressure. The values of $\boldsymbol{\Pi}_0$, Δ_0, and $\mathbf{Q}_0$ are determined by the linear Newtonian law of shear and bulk viscosity, and the linear Fourier law of heat conduction, respectively, given in (2.14). The constant *c*, which is given by $c = \left[{}^{2\sqrt{\pi}}\!/_{5}\, A_2(\nu)\Gamma\left(4 - {}^{2}\!/_{\nu-1}\right)\right]^{1/2}$, has a value between 1.0138 (Maxwellian) and 1.2232 ($\nu = 3$); for instance, 1.018 for the nitrogen gas molecule [8,10]. The tabulated values of $A_2(\nu)$ are available in the literature [77].

The relationships in the second-order Boltzmann-Curtiss-based constitutive model (2.19) are highly non-linear due to the second-order term of kinematic nature $\left[\hat{\boldsymbol{\Pi}}\cdot\nabla\hat{\mathbf{u}}\right]^{(2)}$ and the hyperbolic sine term of dissipative nature $q_{2\mathrm{nd}}(c\hat{R})$. Besides, these algebraic equations are tightly-coupled through the second-order kinematic term $\left[\hat{\boldsymbol{\Pi}}\cdot\nabla\hat{\mathbf{u}}\right]^{(2)}$ and the cumulant $\hat{R}$ in $q_{2\mathrm{nd}}(c\hat{R})$, which represents the contribution from all non-conserved variables in the dissipation. Hence, these equations are named the *nonlinear coupled constitutive relations* (NCCR).

Note also that, once $q_{2\mathrm{nd}}$ is taken first-order closure, that is, $q_{1\mathrm{st}} = 1$, and all coupled terms in the left-hand side of (2.18) are neglected, the corresponding constitutive models exactly recover the NF models (2.14). The physical properties of monatomic, diatomic, and polyatomic gases are illustrated in Table I.

TABLE I. Physical properties of monatomic, diatomic, and polyatomic gases.

Gases	Specific heat ratio (γ)	Bulk visocisty ratio (f_b)	Prandtl number (Pr)	Viscosity index (s)	Gas constant (R)	Viscosity coefficient (μ_{ref})
Argon	1.667	0.0	0.667	0.81	208.24	2.117×10^{-5}
Nitrogen	1.4	0.8	0.7368	0.74	296.91	1.656×10^{-5}
Carbon dioxide	1.2985	1000	0.777	0.93	188.87	1.38×10^{-5}

2.5 Decomposed computation of the multi-dimensional second-order constitutive model

In general, the second-order Boltzmann-Curtiss-based constitutive relations (2.19) consist of 10 implicit algebraic equations of the non-conserved variables ($\Pi_{xx}, \Pi_{xy}, \Pi_{xz}, \Pi_{yy}, \Pi_{yz}, \Pi_{zz}$, Δ, Q_x, Q_y, Q_z) for known 14 parameters of conserved variables (p, T, ∇u, ∇v, ∇w). Because of their highly nonlinear and coupled nature, it appears to be a daunting task to develop a proper numerical method for solving the nonlinear system of equations in multi-dimensional flow problems. Nevertheless, the second-order constitutive relations (2.19) can be rather efficiently solved based on the concept of decomposition and the method of iterations initially proposed by Myong [9].

2.5.1. Two fundamental sub-problems in the second-order constitutive model: compression-expansion and velocity-shear

2.5.1.1. Compression-expansion: the first solver

In the compression-expansion problem, for example, the one-dimensional shock structure problem, where the flow evolves only in one direction (x), the second-order Boltzmann-Curtiss-based constitutive relations (2.19) are reduced to the equations of $\hat{\Pi}_{xx}, \hat{\Delta}, \hat{Q}_x$,

$$\begin{aligned}\hat{\Pi}_{xx} q_{2nd}(c\hat{R}) &= \left(1+ f_b\hat{\Delta} + \hat{\Pi}_{xx}\right)\hat{\Pi}_{xx_0},\\ \hat{\Delta} q_{2nd}(c\hat{R}) &= \left(1+3\left(f_b\hat{\Delta} + \hat{\Pi}_{xx}\right)\right)\hat{\Delta}_0,\\ \hat{Q}_x q_{2nd}(c\hat{R}) &= \left(1+ f_b\hat{\Delta} + \hat{\Pi}_{xx}\right)\hat{Q}_{x_0},\end{aligned} \tag{2.21}$$

where

$$\hat{R}^2 = \frac{3}{2}\hat{\Pi}_{xx}^2 + 2\gamma' f_b\hat{\Delta}^2 + \hat{Q}_x^2. \tag{2.22}$$

In this *x*-directional flow, the driving forces are defined by the gradient of *x*-velocity, $\hat{\Pi}_{xx_0}$ due to $u_x(\equiv \partial u/\partial x)$, and the gradient of temperature, $\hat{Q}_{x_0}$ due to $T_x(\equiv \partial T/\partial x)$. From the first-order Navier law (2.14), we also obtain

$$\hat{\Delta}_0 = \frac{3}{4}\hat{\Pi}_{xx_0}.$$

When the first two components of the equations in (2.21) are divided by each other, the nonlinear coupling factor $q_{2\text{nd}}(c\hat{R})$ and the driving force $\hat{\Pi}_{xx_0}$ are cancelled out, leaving only a common kinematic viscous stress constraint between the *xx*-component of the shear stress and the excess normal stress,

$$\hat{\Delta} = \frac{1}{8 f_b}\left[\left(9 f_b - 4\right)\hat{\Pi}_{xx} - 4 + \sqrt{\left(81 f_b^{\,2} + 72 f_b + 16\right)\hat{\Pi}_{xx}^2 + \left(32 - 24 f_b\right)\hat{\Pi}_{xx} + 16}\right]. \tag{2.23}$$

Figure 1 shows the topology of the zeroth-order, first-order, and second-order solutions of the Boltzmann-Curtiss-based constitutive model for three values of f_b in compression-expansion flow. A cross section of the topology of the viscous normal stress is defined by $\hat{Q}_{x_0} = 0$ or zero thermal force. The topology of the first-order constitutive model is linear to the driving (stress and thermal) forces. The viscous stress is a function of the stress force but is independent of the thermal force. In contrast,

the topology of the second-order Boltzmann-Curtiss-based constitutive model becomes highly nonlinear for all cases as gases are away from thermal equilibrium. Moreover, the topology becomes strongly coupled to the stress and thermal components, and the viscous stress varies nonlinearly with respect to the thermal force, although it is more influenced by the stress force. Further, the topology becomes non-symmetric, resulting in a drastic difference in compression (positive stress force) and expansion (negative stress force) in gases far from thermal non-equilibrium. Even though the details of the second-order model are different for types of gases (monatomic, diatomic, polyatomic), the general patterns remain unchanged.

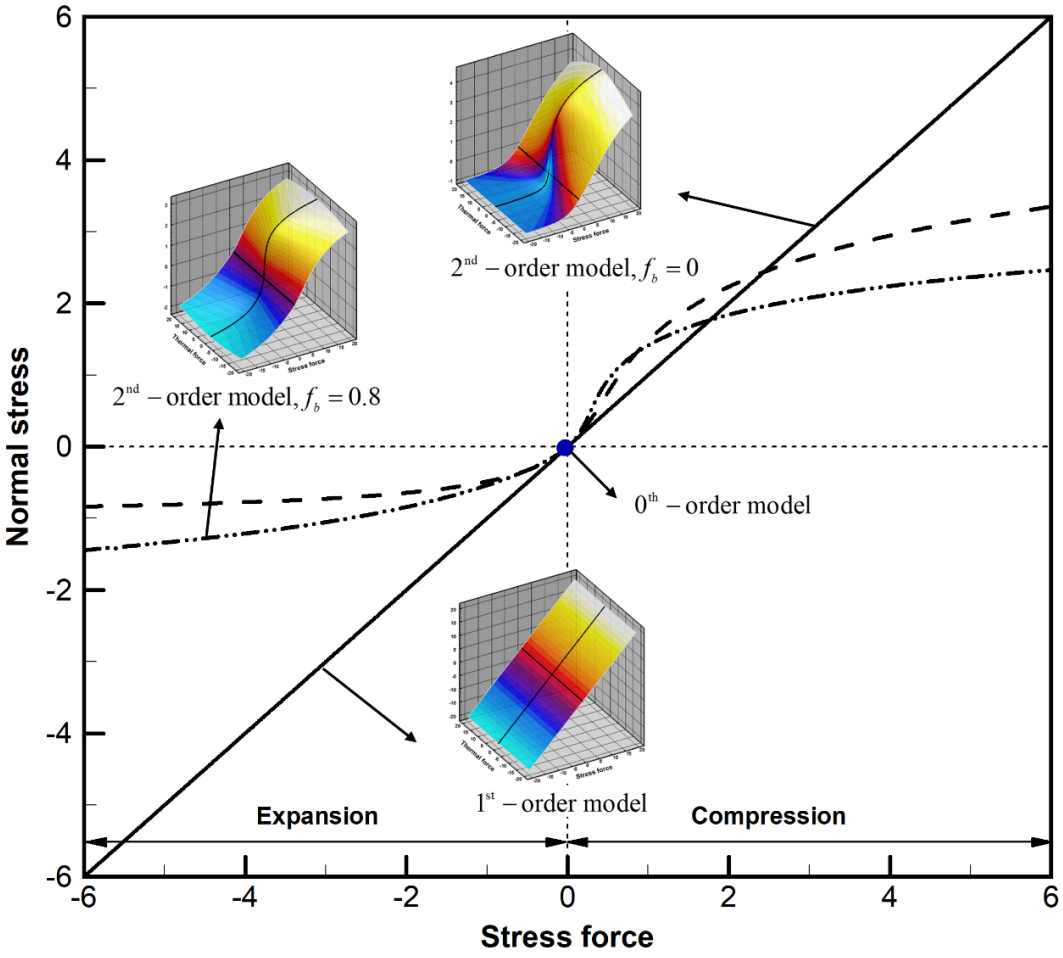

Fig. 1. Topology of zeroth-order, first-order, and second-order solutions of the Boltzmann-Curtiss-based constitutive model for two values of f_b in compression-expansion flow. A cross section of the topology is defined by zero thermal force. The horizontal axis represents the driving stress force $\hat{\Pi}_{xx_0}$, while the vertical axis represents the normal stress $\hat{\Pi}_{xx}$.

2.5.1.2. Velocity-shear flow: the second and third solvers

In the velocity-shear flow problem, in which the flow only evolves in one-direction and the temperature gradients are absent, the second-order Boltzmann-Curtiss-based constitutive relations (2.19) are reduced to the equations of $\hat{\Pi}_{xx}, \hat{\Pi}_{xy}, \hat{\Delta}$,

$$\begin{aligned} \hat{\Pi}_{xx} q_{2nd}(c\hat{R}) &= -\frac{2}{3}\hat{\Pi}_{xy}\hat{\Pi}_{xy_0}, \\ \hat{\Pi}_{xy} q_{2nd}(c\hat{R}) &= \left(1 + f_b\hat{\Delta} + \hat{\Pi}_{xx}\right)\hat{\Pi}_{xy_0}, \\ \hat{\Delta} q_{2nd}(c\hat{R}) &= 3\hat{\Pi}_{xy}\hat{\Pi}_{xy_0}. \end{aligned} \tag{2.24}$$

Here the flow is assumed to be driven by the gradient of *y*-velocity in the *x*-direction, $v_x (\equiv \partial v / \partial x)$, that is, $\hat{\Pi}_{xy_0}$. After some manipulation, the following equations on variables $\hat{\Pi}_{xx}$ and $\hat{\Delta}$ can be derived,

$$\begin{aligned} \hat{\Pi}_{xx} q_{2nd}^2(c\hat{R}) &= -\frac{2}{3}\left[\left(1 - \frac{9}{2} f_b\right)\hat{\Pi}_{xx} + 1\right]\hat{\Pi}_{xy_0}^2, \\ \hat{\Delta} &= -\frac{9}{2}\hat{\Pi}_{xx}. \end{aligned} \tag{2.25}$$

Furthermore, when the first two components of the equations in (2.24) are divided by each other, the nonlinear coupling factor $q_{2nd}(c\hat{R})$ and the driving force $\hat{\Pi}_{xy_0}$ are cancelled out, leaving only a common kinematic viscous stress constraint:

$$\frac{2}{3}\hat{\Pi}_{xy}^2 + \left(1 - \frac{9}{2} f_b\right)\hat{\Pi}_{xx}^2 + \hat{\Pi}_{xx} = 0, \text{ or } \hat{\Pi}_{xy} = \text{sign}\left(\hat{\Pi}_{xy_0}\right)\left\{-\frac{3}{2}\left[\left(1 - \frac{9}{2} f_b\right)\hat{\Pi}_{xx} + 1\right]\hat{\Pi}_{xx}\right\}^{1/2}. \tag{2.26}$$

Combining all these relations, the dissipation function reduces to

$$\hat{R}^2 = 3\hat{\Pi}_{xx}\left[\left(1 + \frac{9}{2} f_b\left(1 + 3\gamma'\right)\right)\hat{\Pi}_{xx} - 1\right]. \tag{2.27}$$

The third solver of $\hat{\Pi}_{xx}, \hat{\Pi}_{xz}, \hat{\Delta}$ for the driving force $w_x (\equiv \partial w / \partial x)$ can be developed in a similar fashion.

Figure 2 illustrates the topology of the second-order solution of the Boltzmann-Curtiss-based constitutive model in the velocity-shear flow problem (2.26) in a phase space (Π_{xx}, Π_{xy}, p). It is an ellipse cone for $f_b = 0$, while it is a hyperboloid for $f_b = 1$. For a monatomic gas ($f_b = 0$), a similar type of ellipse cone was identified in the context of a phase-transition-like behaviour in velocity slips in a cylindrical Couette flow [80]. As the pressure decreases, the ellipse cone keeps its topology, whereas the hyperboloid approaches a different topology of straight lines.

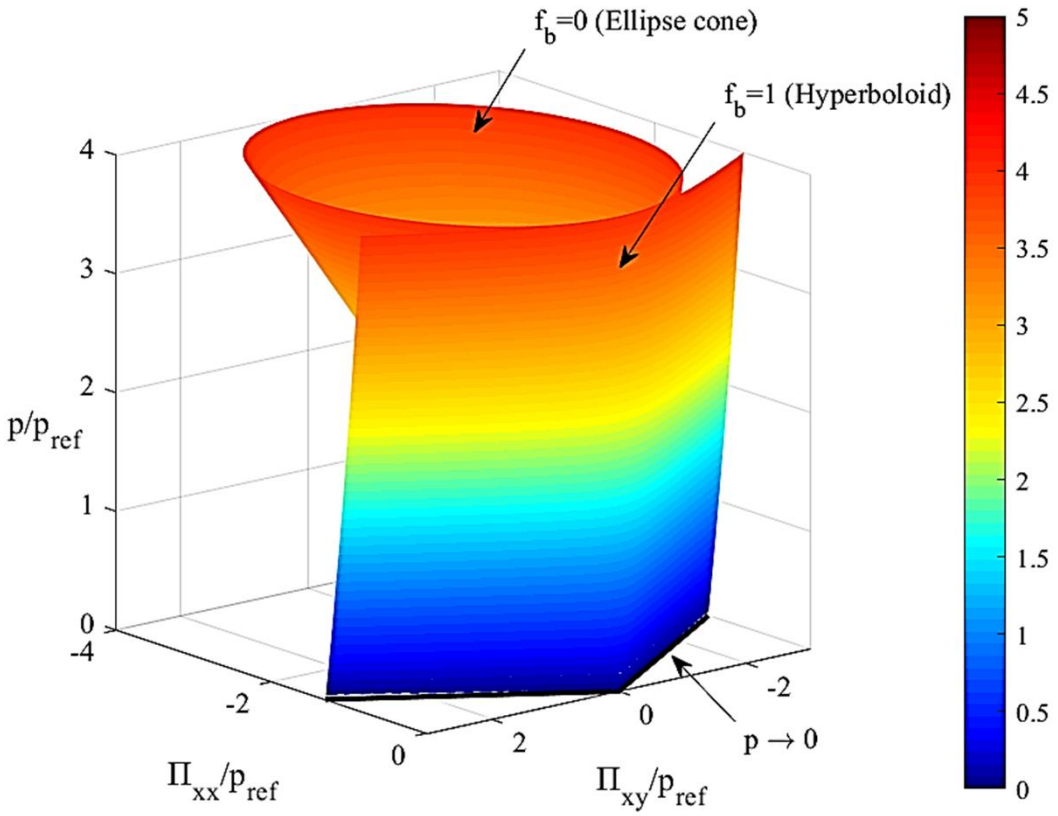

FIG. 2. Topology of the second-order Boltzmann-Curtiss-based constitutive model in the velocity shear flow problem in a phase space (Π_{xx}, Π_{xy}, p) for $f_b = 0$ and $f_b = 1$. (Reproduced with permission from Singh *et al.*, "Topology of the second-order constitutive model based on the Boltzmann–Curtiss kinetic equation for diatomic and polyatomic gases," Phys. Fluids 32, 026104 (2020). Copyright 2020 AIP).

Figure 3 shows the zeroth-, first-, and second-order velocity-shear flow solutions of the Boltzmann-Curtiss-based constitutive model for a driving stress force in monatomic, diatomic, and polyatomic gases. The viscous shear stress $\hat{\Pi}_{xy}$ computed using the second-order constitutive model recovers the first-order model near the origin, but it becomes highly nonlinear as the stress force (shear velocity gradient) increases. The second-order constitutive model displays shear-thinning characteristics, yielding a smaller shear stress compared to the first-order constitutive model. Furthermore, it produces non-zero normal stress values for a velocity gradient in shear flow, which is in stark contrast with the first-order constitutive model. Interestingly, the general solutions of the second-order constitutive model also show asymptotic behaviour with the increasing degree of velocity shear, satisfying the free-molecular limit $\hat{\Pi}_{xx} + \hat{\Delta} \to -1$ or $\Pi_{xx} + \Delta + p \to 0$ in the conservation laws (2.7).

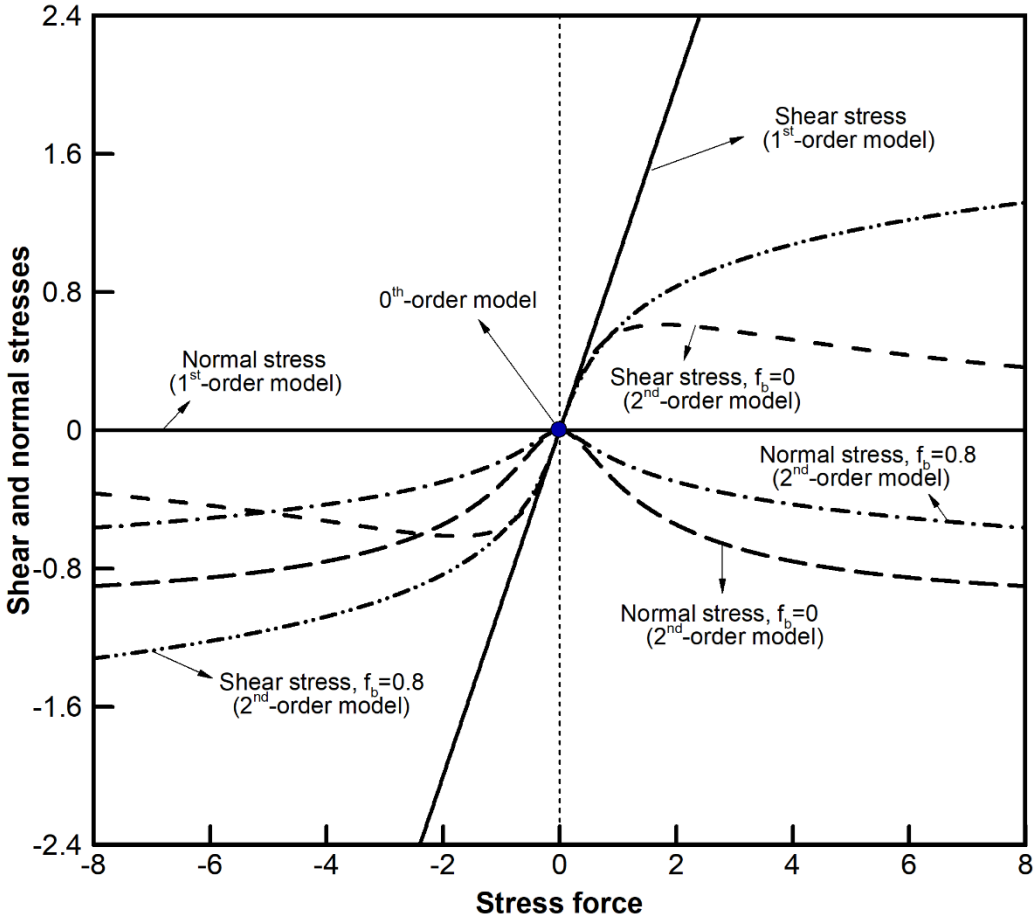

Fig. 3. Zeroth-, first-, and second-order velocity-shear flow solutions of the Boltzmann-Curtiss based constitutive model for a driving stress force in monatomic, diatomic, and polyatomic gases.

The horizontal axis represents the driving stress force $\hat{\Pi}_{xy_0}$, while the vertical axis represents the shear and normal stresses $\hat{\Pi}_{xy}, \hat{\Pi}_{xx}$.

2.5.2. Decomposition of the multi-dimensional second-order constitutive model in the surface integral

The three-dimensional flow problem can be split into three sub-problems in the x, y, z directions. The stress and heat flux components $(\Pi_{xx}, \Pi_{xy}, \Pi_{xz}, \Delta, Q_x)$ on a surface in a three-dimensional control volume induced by thermodynamic driving forces such as velocity gradients (u_x, v_x, w_x) and temperature gradients (T_x) can be approximated as the sum of three decomposed solvers; first on $(u_x, 0, 0, T_x)$ describing the compression-expansion flow, second on $(0, v_x, 0, 0)$, and third on $(0, 0, w_x, 0)$ describing the velocity-shear flow. Hence, the non-conservative variables in the case of *x*-direction can be decomposed as follows,

$$f(u_x, v_x, w_z, T_x) = f_1(u_x, 0, 0, T_x) + f_2(0, v_x, 0, 0) + f_3(0, 0, w_x, 0). \tag{2.28}$$

Similarly, it is possible to calculate the stress and heat flux in two other primary directions. For the *y*- and *z*-directions, the non-conservative variables can be decomposed as follows, respectively,

$$g(u_y, v_y, w_y, T_y) = g_1(0, v_y, 0, T_y) + g_2(u_y, 0, 0, 0) + g_3(0, 0, w_y, 0), \tag{2.29}$$

$$h(u_z, v_z, w_z, T_z) = h_1(0, 0, w_z, T_z) + h_2(u_z, 0, 0, 0) + h_3(0, v_z, 0, 0). \tag{2.30}$$

Since *x*, *y*, and *z* are the primary directions in Eqs. (2.28), (2.29)-(2.30), respectively, the corresponding solver components $f_1, f_2, f_3, g_1, g_2, g_3, h_1, h_2, h_3$ can be computed as summarized in Table 2.

Table 2 Components of the three-dimensional decomposed solver and their corresponding computed non-conserved variables

Components of decomposed solver	Corresponding non-conserved variables
$f_1(u_x,0,0,T_x)$	$\Pi_{xx-1x},\ \Pi_{xy-1x}=0,\ \Pi_{xz-1x}=0,\ \Pi_{yy-1x}=-\Pi_{xx-1x}/2,\ \Pi_{yz-1x}=0,\ \Pi_{zz-1x}=-\Pi_{xx-1x}/2,$ $Q_{1x}=Q_x,\ \Delta_{1x}$
$f_2(0,v_x,0,0)$	$\Pi_{xx-2x},\ \Pi_{xy-2x},\ \Pi_{xz-2x}=0,\ \Pi_{yy-2x}=-2\Pi_{xx-2x},\ \Pi_{zz-2x}=\Pi_{xx-2x},\ \Pi_{yz-2x}=0,$ $Q_{2x}=0,\ \Delta_{2x}$
$f_3(0,0,w_x,0)$	$\Pi_{xx-3x},\ \Pi_{xy-3x}=0,\ \Pi_{xz-3x},\ \Pi_{yy-3x}=\Pi_{xx-3x},\ \Pi_{zz-3x}=-2\Pi_{xx-3x},\ \Pi_{yz-3x}=0,$ $Q_{3x}=0,\ \Delta_{3x}$
$g_1(0,v_y,0,T_y)$	$\Pi_{xx-1y}=-\Pi_{yy-1y}/2,\ \Pi_{xy-1y}=0,\ \Pi_{yy-1y},\ \Pi_{xz-1y}=0,\ \Pi_{yz-1y}=0,\ \Pi_{zz-1y}=-\Pi_{yy-1y}/2,$ $Q_{1y}=Q_y,\ \Delta_{1y}$
$g_2(u_y,0,0,0)$	$\Pi_{xx-2y}=-2\Pi_{yy-2y},\ \Pi_{xy-2y},\ \Pi_{xz-2y}=0,\ \Pi_{yy-2y},\ \Pi_{yz-2y}=0,\ \Pi_{zz-2y}=\Pi_{yy-2y},$ $Q_{2y}=0,\ \Delta_{2y}$
$g_3(0,0,w_y,0)$	$\Pi_{xx-3y}=\Pi_{yy-3y},\ \Pi_{xy-3y}=0,\ \Pi_{xz-3y}=0,\ \Pi_{yy-3y},\ \Pi_{zz-3y}=-2\Pi_{yy-3y},\ \Pi_{yz-3y},$ $Q_{3y}=0,\ \Delta_{3y}$
$h_1(0,0,w_z,T_z)$	$\Pi_{xx-1z}=-\Pi_{zz-1z}/2,\ \Pi_{xy-1z}=0,\ \Pi_{xz-1z}=0,\ \Pi_{yy-1z}=-\Pi_{zz-1z}/2,\ \Pi_{yz-1z}=0,\ \Pi_{zz-1z},$ $Q_{1z}=Q_z,\ \Delta_{1z}$
$h_2(u_z,0,0,0)$	$\Pi_{xx-2z}=-2\Pi_{zz-2z},\ \Pi_{xy-2z}=0,\ \Pi_{xz-2z},\ \Pi_{yy-2z}=\Pi_{zz-2z},\ \Pi_{yz-2z}=0,\ \Pi_{zz-2z},$ $Q_{2z}=0,\ \Delta_{2z}$
$h_3(0,v_z,0,0)$	$\Pi_{xx-3z}=-2\Pi_{zz-3z},\ \Pi_{xy-3z}=0,\ \Pi_{xz-3z}=0,\ \Pi_{yy-3z}=-2\Pi_{zz-3z},\ \Pi_{yz-3z},\ \Pi_{zz-3z},$ $Q_{3z}=0,\ \Delta_{3z}$

Finally, all non-conserved variables can be determined by adding up all these contributions from the decomposed solvers as

$$
\begin{aligned}
&\Pi_{xx} = \Pi_{xx-1x} + \Pi_{xx-2x} + \Pi_{xx-3x} - \frac{1}{2}\left(\Pi_{yy-1y} + \Pi_{zz-1z}\right) - 2\left(\Pi_{yy-2y} + \Pi_{zz-2z}\right) + \Pi_{yy-3y} + \Pi_{zz-3x}, \\
&\Pi_{yy} = \Pi_{yy-1y} + \Pi_{yy-2y} + \Pi_{yy-3y} - \frac{1}{2}\left(\Pi_{xx-1x} + \Pi_{zz-1z}\right) - 2\left(\Pi_{xx-2x} + \Pi_{zz-3z}\right) + \Pi_{zz-2z} + \Pi_{xx-3x}, \\
&\Pi_{zz} = \Pi_{zz-1z} + \Pi_{zz-2z} + \Pi_{zz-3z} - \frac{1}{2}\left(\Pi_{xx-1x} + \Pi_{yy-1y}\right) - 2\left(\Pi_{xx-3x} + \Pi_{yy-3y}\right) + \Pi_{xx-2x} + \Pi_{yy-2y}, \\
&\Pi_{xy} = \Pi_{xy-2x} + \Pi_{xy-2y}, \\
&\Pi_{xz} = \Pi_{xz-3x} + \Pi_{xz-2z}, \\
&\Pi_{yz} = \Pi_{yz-3y} + \Pi_{yz-3z}, \\
&Q_x = Q_{1x},\ Q_y = Q_{1y},\ Q_z = Q_{1z}, \\
&\Delta = \Delta_{1x} + \Delta_{2x} + \Delta_{3x} + \Delta_{1y} + \Delta_{2y} + \Delta_{3y} + \Delta_{1z} + \Delta_{2z} + \Delta_{3z}.
\end{aligned}
\tag{2.31}
$$

Note that (2.31) satisfies the traceless property of the viscous stress tensor, i.e., $\Pi_{xx} + \Pi_{yy} + \Pi_{zz} = 0$. The concept of decomposition of second-order constitutive relations for multi-dimensional flows in the surface integral is depicted in Fig. 4.

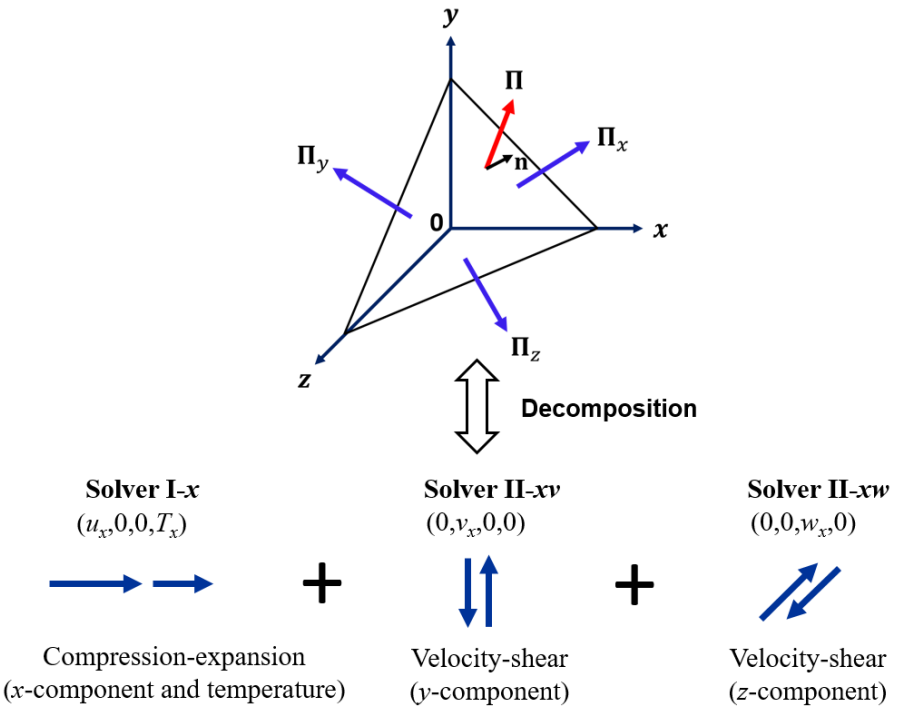

Fig. 4. Concept of decomposition of second-order constitutive relations for multi-dimensional flow in the primary surface integral: compression-expansion (*x*-component), velocity-shear flow (*y*-component), and velocity-shear flow (z-component).

2.5.3. Decomposition of the multi-dimensional second-order constitutive model in the volume integral

In contrast to the finite volume formulation where only the surface integral is required, the DG formulation requires the volume integral. To decompose the second-order constitutive relations for multi-dimensional flows in the volume integral, the viscous flux in (2.10) is divided into three terms,

$$\mathbf{F}^{\text{vis}} = \mathbf{F}_x^{\text{vis}} + \mathbf{F}_y^{\text{vis}} + \mathbf{F}_z^{\text{vis}} \tag{2.32}$$

where $\mathbf{F}_x^{\text{vis}}, \mathbf{F}_y^{\text{vis}}$, and $\mathbf{F}_z^{\text{vis}}$ are defined in dimensional form as,

$$\mathbf{F}_x^{\text{vis}} = \begin{bmatrix} 0 \\ \Pi_{xx} + \Delta_x \\ \Pi_{xy} \\ \Pi_{xz} \\ \left(\Pi_{xx} + \Delta_x\right)u + \Pi_{xy}v + \Pi_{xz}w + Q_x \end{bmatrix}, \quad \mathbf{F}_y^{\text{vis}} = \begin{bmatrix} 0 \\ \Pi_{xy} \\ \Pi_{yy} + \Delta_y \\ \Pi_{yz} \\ \Pi_{xy}u + \left(\Pi_{yy} + \Delta_y\right)v + \Pi_{yz}w + Q_y \end{bmatrix}, \tag{2.33}$$

$$\mathbf{F}_z^{\text{vis}} = \begin{bmatrix} 0 \\ \Pi_{xz} \\ \Pi_{yz} \\ \Pi_{zz} + \Delta_z \\ \Pi_{xz}u + \Pi_{yz}v + \left(\Pi_{zz} + \Delta_z\right)w + Q_z \end{bmatrix}.$$

In the *x*-direction, the viscous flux $\mathbf{F}_x^{\text{vis}}$ can be decomposed into primary (*P*) and secondary (*S*) parts,

$$\mathbf{F}_x^{\text{vis}} = \begin{bmatrix} 0 \\ \Pi_{xx_P} + \Delta_{x_P} \\ \Pi_{xy_P} \\ \Pi_{xz_P} \\ \left(\Pi_{xx_P} + \Delta_{x_P}\right)u + \Pi_{xy_P}v + \Pi_{xz_P}w + Q_{x_P} \end{bmatrix}_P + \begin{bmatrix} 0 \\ \Pi_{xx_S} + \Delta_{x_S} \\ \Pi_{xy_S} \\ \Pi_{xz_S} \\ \left(\Pi_{xx_S} + \Delta_{x_S}\right)u + \Pi_{xy_S}v + \Pi_{xz_S}w \end{bmatrix}_S. \tag{2.34}$$

The primary and secondary parts of the viscous flux can be further decomposed into seven sub-parts,

$$\mathbf{F}_x^{\text{vis}} = \begin{bmatrix} 0 \\ \Pi_{xx_{P1}} + \Delta_{x_{P1}} \\ 0 \\ 0 \\ \left(\Pi_{xx_{P1}} + \Delta_{x_{P1}}\right)u + Q_{x_{P1}} \end{bmatrix}_{P1x} + \begin{bmatrix} 0 \\ \Pi_{xx_{P2v}} + \Delta_{x_{P2v}} \\ \Pi_{xy_{P2v}} \\ 0 \\ \left(\Pi_{xx_{P2v}} + \Delta_{x_{P2v}}\right)u + \Pi_{xy_{P2v}} v \end{bmatrix}_{P2xv} + \tag{2.35}$$

$$\begin{bmatrix} 0 \\ \Pi_{xx_{P2w}} + \Delta_{x_{P2w}} \\ 0 \\ \Pi_{xz_{P2w}} \\ \left(\Pi_{xx_{P2w}} + \Delta_{x_{P2w}}\right)u + \Pi_{xz_{P2w}} w \end{bmatrix}_{P2xw} + \begin{bmatrix} 0 \\ \Pi_{xx_{S1v}} + \Delta_{x_{S1v}} \\ 0 \\ 0 \\ \left(\Pi_{xx_{S1v}} + \Delta_{x_{S1v}}\right)u \end{bmatrix}_{S1xv} + \begin{bmatrix} 0 \\ \Pi_{xx_{S1w}} + \Delta_{x_{S1w}} \\ 0 \\ 0 \\ \left(\Pi_{xx_{S1w}} + \Delta_{x_{S1w}}\right)u \end{bmatrix}_{S1xw} +$$

$$\begin{bmatrix} 0 \\ \Pi_{xx_{S2v}} + \Delta_{x_{S2v}} \\ \Pi_{xy_{S2v}} \\ 0 \\ \left(\Pi_{xx_{S2v}} + \Delta_{x_{S2v}}\right)u + \Pi_{xy_{S2v}} v \end{bmatrix}_{S2xv} + \begin{bmatrix} 0 \\ \Pi_{xx_{S2w}} + \Delta_{x_{S2w}} \\ 0 \\ \Pi_{xz_{S2w}} \\ \left(\Pi_{xx_{S2w}} + \Delta_{x_{S2w}}\right)u + \Pi_{xz_{S2w}} w \end{bmatrix}_{S2xw} .$$

The seven sub-parts recover the following form in the limit of the first-order NF constitutive relation near LTE, respectively,

$$\begin{bmatrix} 0 \\ -\frac{4}{3}\mu u_x - \mu_b u_x \\ 0 \\ 0 \\ \left(-\frac{4}{3}\mu u_x - \mu_b u_x\right)u - kT_x \end{bmatrix}_{P1x} + \begin{bmatrix} 0 \\ 0 \\ -\mu v_x \\ 0 \\ -\mu v_x v \end{bmatrix}_{P2xv} + \begin{bmatrix} 0 \\ 0 \\ 0 \\ -\mu w_x \\ -\mu w_x w \end{bmatrix}_{P2xw} + \tag{2.36}$$

$$\begin{bmatrix} 0 \\ \frac{2}{3}\mu v_y - \mu_b v_y \\ 0 \\ 0 \\ \left(\frac{2}{3}\mu v_y - \mu_b v_y\right)u \end{bmatrix}_{S1xv} + \begin{bmatrix} 0 \\ \frac{2}{3}\mu w_z - \mu_b w_z \\ 0 \\ 0 \\ \left(\frac{2}{3}\mu w_z - \mu_b w_z\right)u \end{bmatrix}_{S1xw} + \begin{bmatrix} 0 \\ 0 \\ -\mu u_y \\ 0 \\ -\mu u_y v \end{bmatrix}_{S2xv} + \begin{bmatrix} 0 \\ 0 \\ 0 \\ -\mu u_z \\ -\mu u_z w \end{bmatrix}_{S2xw} .$$

The seven sub-parts (2.36) can be written in the following non-conservative form of solvers,

$$\left(-\frac{4}{3}\mu u_x,0,0,-kT_x\right)_{P1x},\ (0,-\mu v_x,0,0)_{P2xv},\ (0,0,-\mu w_x,0)_{P2xw},$$
$$\left(\frac{2}{3}\mu v_y,0,0,0\right)_{S1xv},\ \left(\frac{2}{3}\mu w_z,0,0,0\right)_{S1xw},\ (0,-\mu u_y,0,0)_{S2xv},\ (0,0,-\mu u_z,0)_{S2xw}. \tag{2.37}$$

Note that the driving forces v_z, w_y are not present in (2.36) and (2.37) since they do not contribute to the x-component of viscous flux $\mathbf{F}_x^{\text{vis}}$. The concept of decomposition of second-order constitutive relations for multi-dimensional flows in the volume integral is depicted in Fig. 5.

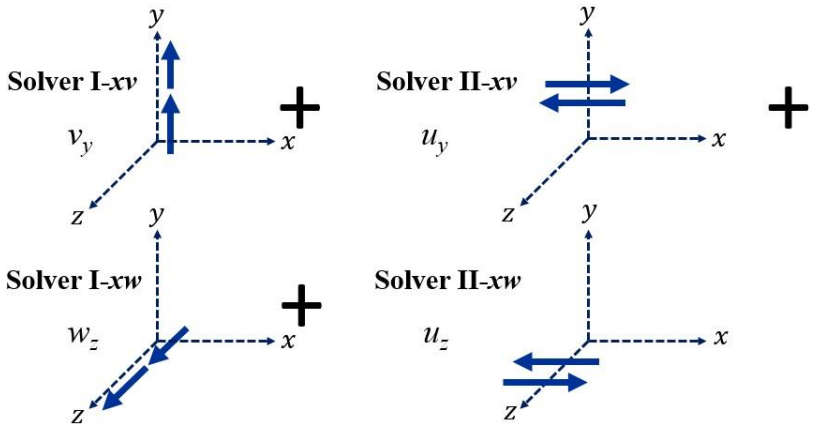

Fig. 5. Concept of decomposition of second-order constitutive relations for multi-dimensional flow in the secondary volume integral.

For the secondary part $S1xv$ in the seven sub-parts (2.37), the solver of $(\hat{\Pi}_{xx_{S1x}},\hat{\Delta}_{S1x})$ for the driving force $(2\mu v_y/3,0,0,0)$, which physically represents the compression-expansion flow without the heat flux, can be summarized as

$$\hat{\Pi}_{xx_{S1x}} = -\frac{1}{2}\hat{\Pi}_{yy_{S1x}},$$
$$\hat{\Pi}_{xx0_{S1x}} = -\frac{1}{3}\hat{v}_y, \tag{2.38}$$

where $\hat{\Pi}_{yy_{S1x}}$ and $\hat{\Delta}_{S1x}$ are determined by

$$\hat{\Pi}_{yy_{S1x}}\, q_{2nd}(c\hat{R}) = \left(1+ f_b\hat{\Delta}_{S1x} + \hat{\Pi}_{yy_{S1x}}\right)\hat{\Pi}_{yy0_{S1x}},$$
$$\hat{\Delta}_{S1x}\, q_{2nd}(c\hat{R}) = \left(1+3\left(f_b\hat{\Delta}_{S1x} + \hat{\Pi}_{yy_{S1x}}\right)\right)\hat{\Delta}_{0_{S1x}},$$
$$\hat{R}^2 = \frac{3}{2}\hat{\Pi}^2_{yy_{S1x}} + 2\gamma' f_b\hat{\Delta}^2_{S1x},$$
$$\hat{\Pi}_{yy0_{S1x}} = -2\hat{\Pi}_{xx0_{S1x}},\ \hat{\Delta}_{0_{S1x}} = \frac{3}{4}\hat{\Pi}_{yy0_{S1x}} = -\frac{3}{2}\hat{\Pi}_{xx0_{S1x}}. \tag{2.39}$$

For the secondary part $S2xv$, the solver of $(\hat{\Pi}_{xx_{S2x}}, \hat{\Pi}_{xy_{S2x}}, \hat{\Delta}_{S2x})$ for the driving force $(0, -\mu u_y, 0, 0)$, which physically represents the velocity-shear flow, can be summarized as

$$\hat{\Pi}_{xx_{S2x}} = -2\hat{\Pi}_{yy_{S2x}}$$
$$\hat{\Pi}_{xy0_{S2x}} = \frac{1}{2}\hat{u}_y, \tag{2.40}$$

where $\hat{\Pi}_{xy_{S2x}}$, $\hat{\Pi}_{yy_{S2x}}$ and $\hat{\Delta}_{S2x}$ are determined by

$$\hat{\Pi}_{yy_{S2x}}\, q_{2nd}(c\hat{R}) = -\frac{2}{3}\hat{\Pi}_{yy_{S2x}}\hat{\Pi}_{xy0_{S2x}},$$
$$\hat{\Pi}_{xy_{S2x}}\, q_{2nd}(c\hat{R}) = \left(1+\hat{\Pi}_{yy_{S2x}} + f_b\hat{\Delta}_{S2x}\right)\hat{\Pi}_{xy0_{S2x}},$$
$$\hat{\Delta}_{S2x}\, q_{2nd}(c\hat{R}) = 3\hat{\Pi}_{xy_{S2x}}\hat{\Pi}_{xy0_{S2x}},$$
$$\hat{R}^2 = 3\hat{\Pi}^2_{yy_{S2x}}\left[\left(1+\frac{9}{2} f_b\left(1+3\gamma'\right)\right)\hat{\Pi}_{yy_{S2x}} - 1\right]. \tag{2.41}$$

After employing the second-order constitutive model, the viscous flux $\mathbf{F}_x^{\text{vis}}$ in Eq. (2.34) can be determined by summing up the primary and secondary parts. The viscous flux in the *y*- and *z*-directions can be determined in similar fashion.

2.5.4. Algorithms based on an iterative method

The iteration procedure can be developed individually for the decomposed solvers as follows [8-10]. In the first solver on $(u_x, 0, 0, T_x)$ described in subsection 2.5.1.1, which represents the compression-expansion flow, the stresses and heat flux (Π_{xx}, Δ, Q_x) for positive $\hat{\Pi}_{xx_0}$ and $\hat{Q}_{x_0}$ can be determined by the following iterations,

$$\hat{\Pi}_{xx_{n+1}} = \frac{\left(1+ f_b\hat{\Delta}_n + \hat{\Pi}_{xx_n}\right)\hat{\Pi}_{xx_0}}{\sqrt{Y_n}}\hat{R}_{n+1},\ \ \hat{Q}_{x_{n+1}} = \frac{\hat{Q}_{x_0}}{\hat{\Pi}_{xx_0}}\hat{\Pi}_{xx_{n+1}}, \tag{2.42}$$

where

$$\begin{aligned}&\hat{R}_{n+1} = \frac{1}{c}\sinh^{-1}\left(c\sqrt{Y_n}\right),\\ &Y_n = \left(1+ f_b\hat{\Delta}_n + \hat{\Pi}_{xx_n}\right)^2\hat{R}_0^2 + 4\left(f_b\hat{\Delta}_n + \hat{\Pi}_{xx_n}\right)\left(1+2\left(f_b\hat{\Delta}_n + \hat{\Pi}_{xx_n}\right)\right)2\gamma' f_b\hat{\Delta}_0^2.\end{aligned} \tag{2.43}$$

For negative $\hat{\Pi}_{xx_0}$ and $\hat{Q}_{x_0}$, the stresses and heat flux are determined by the following iterations,

$$\hat{\Pi}_{xx_{n+1}} = \frac{\left(1+ f_b\hat{\Delta}_n\right)\hat{\Pi}_{xx_0}}{q_{2nd}\left(c\hat{R}_n\right) - \hat{\Pi}_{xx_0}},\ \ \hat{Q}_{x_{n+1}} = \frac{\hat{Q}_{x_0}}{\hat{\Pi}_{xx_0}}\hat{\Pi}_{xx_{n+1}}. \tag{2.44}$$

In both cases, the following relation from (2.23) is used,

$$\hat{\Delta}_n = \frac{1}{8f_b}\left[\left(9f_b - 4\right)\hat{\Pi}_{xx_n} - 4 + \sqrt{\left(81f_b^2 + 72f_b + 16\right)\hat{\Pi}_{xx_n}^2 + \left(32 - 24f_b\right)\hat{\Pi}_{xx_n} + 16}\right].$$

In these expressions, $\hat{\Pi}_{xx_1}, \hat{\Delta}_1, \hat{Q}_{x_1}$ are given by the equations,

$$\hat{\Pi}_{xx_1} = \frac{\sinh^{-1}(c\hat{R}_0)}{c\hat{R}_0}\hat{\Pi}_{xx_0},\ \ \hat{\Delta}_1 = \frac{\sinh^{-1}(c\hat{R}_0)}{c\hat{R}_0}\hat{\Delta}_0,\ \ \hat{Q}_{x_1} = \frac{\sinh^{-1}(c\hat{R}_0)}{c\hat{R}_0}\hat{Q}_{x_0}. \tag{2.45}$$

In the meantime, the solver *S1xv* of compression-expansion flow without the heat flux, which was described in (2.36) and (2.37), can be developed by simply ignoring the heat flux in the present first solver.

In the second solver on $(0, v_x, 0, 0)$ described in subsection 2.5.1.2, which represents the velocity-shear flow, the stresses $\hat{\Pi}_{xx}$ and $\hat{\Pi}_{xy}$ can be calculated for a given $\hat{\Pi}_{xy_0}$ through the kinematic viscous stress constraint (2.26) and the following equations; when $0 \le f_b < 2/9$,

$$\hat{\Pi}_{xx_{n+1}} = -\frac{2\hat{\Pi}_{xy_0}^2}{3q_{2nd}^2\left(c\hat{R}_n\right) + \left(2 - 9f_b\right)\hat{\Pi}_{xy_0}^2}, \quad \hat{R}_n = \left\{3\hat{\Pi}_{xx_n}\left[\left(1 + \frac{9}{2}f_b\left(1 + 3\gamma'\right)\right)\hat{\Pi}_{xx_n} - 1\right]\right\}^{1/2}. \tag{2.46}$$

On the other hand, when $f_b \ge 2/9$, the $\hat{\Pi}_{xx}$ can be calculated using the following iterations,

$$\begin{aligned} &\hat{R}_{n+1} = \frac{1}{c}\sinh^{-1}\left(cY_n\right), \quad \hat{\Pi}_{xx_{n+1}} = \frac{3 - \sqrt{D_{n+1}}}{3\left(2 + 9f_b\left(1 + 3\gamma'\right)\right)}, \\ &Y_n = \left\{2\left[1 + \left(1 - \frac{9}{2}f_b\right)\hat{\Pi}_{xx_n}\right]\left[1 - \left(1 + \frac{9}{2}f_b\left(1 + 3\gamma'\right)\right)\hat{\Pi}_{xx_n}\right]\right\}^{1/2}\hat{\Pi}_{xy_0}, \\ &D_{n+1} = 9 + 6\left(2 + 9f_b\left(1 + 3\gamma'\right)\right)\hat{R}_{n+1}^2. \end{aligned} \tag{2.47}$$

Note that the term Y_n is well defined for any f_b value greater than the critical value $2/9 \approx 0.2222$.

The third solver on $(0, 0, w_x, 0)$ can be developed in similar fashion.

3 Three-dimensional mixed modal discontinuous Galerkin method

3.1 Spatial discretization in the DG framework

The spatial discretization of the conservation laws (2.9) in conjunction with the second-order constitutive models (2.19) cannot be achieved with the standard DG method due to the highly nonlinear and implicit form of the constitutive relations in the viscous and heat flux terms. Therefore, we employ a mixed modal discontinuous Galerkin (DG) formulation developed by Myong and co-authors [15-17,32-34,57,58, 81-84]. In this mixed formulation, a new additional auxiliary variable Θ is introduced to handle the second-order derivatives appearing in the implicit constitutive relations of viscous stress and heat flux. In this method, the auxiliary variable can be defined as the derivative of either primitive

or conservative variables. To apply the mixed DG formulation, Eq. (2.9) can be expressed as a coupled system for $\mathbf{U}$ and Θ as

$$\begin{aligned} \Theta - \nabla \mathbf{U} &= 0, \\ \frac{\partial \mathbf{U}}{\partial t} + \nabla \cdot \mathbf{F}^{inv}\left(\mathbf{U}\right) + \nabla \cdot \mathbf{F}^{vis}\left(\mathbf{U}, \Theta\right) &= 0. \end{aligned} \tag{3.1}$$

In order to discretize the coupled system of equations (3.1), the domain Ω can be approximated by Ω_h such that $\Omega_h \to \Omega$ as $h \to 0$. Accordingly, the approximated domain Ω_h is tessellated into a collection of non-overlapping elements Ω_e such that $\mathcal{T}_h = \{\Omega_e\}$. In this study, the domain is decomposed into unstructured tetrahedral elements. For the domain Ω_h, we introduce the piecewise polynomial space of the functions $v_h : \Omega_h \mapsto \Re$ such that

$$\mathrm{V}_h = \left\{ v_h \in L_2\left(\Omega_h\right) : \quad v_h\big|_{\Omega_e} \in P^k\left(\Omega_e\right), \quad \forall \Omega_e \in \mathcal{T}_h \right\}, \tag{3.2}$$

where $L_2\left(\Omega_h\right)$ denotes the space function of the squared Lebesque integrable over the domain Ω_h and $P^k\left(\Omega_e\right)$ denotes the space of polynomial functions of degree at most k in element Ω_e. To formulate the DG method, the exact solutions of $\mathbf{U}$ and Θ are approximated by the DG polynomial approximation of $\mathbf{U}_h \in \mathrm{V}_h\left(\mathcal{T}_h\right)$ and $\Theta_h \in \mathrm{V}_h\left(\mathcal{T}_h\right)$, respectively,

$$\begin{aligned} \mathbf{U}_h\left(\mathbf{x}, t\right) &= \sum_{i=0}^{N_k} \hat{\mathrm{U}}_h^i\left(t\right) b_i\left(\mathbf{x}\right), \\ \Theta_h\left(\mathbf{x}, t\right) &= \sum_{i=0}^{N_k} \hat{\Theta}_h^i\left(t\right) b_i\left(\mathbf{x}\right), \quad \mathbf{x} \in \Omega_e, \end{aligned} \tag{3.3}$$

where $\hat{\mathrm{U}}_h^i$, $\hat{\Theta}_h^i$ are the local degrees of freedom of $\mathbf{U}$ and Θ, $b_i\left(\mathbf{x}\right)$ is the basis function for the finite element space, and N_k is the number of required basis functions for the k-exact DG approximation, which is given by the following relation

$$N_k = \frac{(k+1)(k+2)(k+3)}{6}.$$

In the present work, hierarchical basis functions based on orthogonal Jacobi polynomials are employed for the tetrahedral elements [84]. They are constructed as a tensor product of the so-called principal functions as

$$b_k(\xi,\eta,\zeta) = \psi_i^a\left(\frac{2\xi}{1-\eta-\zeta}-1\right)\psi_{ij}^b\left(\frac{2\eta}{1-\zeta}-1\right)\psi_{ijk}^c(2\xi-1), \tag{3.4}$$

where the principal functions are defined as,

$$\psi_i^a(z) = P_i^{0,0}(z),\ \psi_{ij}^b(z) = \left(\frac{1-z}{2}\right)^i P_j^{2i+1,0}(z),\ \psi_{ijk}^c(z) = \left(\frac{1-z}{2}\right)^{i+j} P_k^{2i+2j+2,0}(z). \tag{3.5}$$

Here $P_n^{a,b}(m)$ represents the Legendre polynomials. A standard tetrahedral element Ω_e^{st} is defined using a local Cartesian coordinate system $(\xi,\eta,\zeta)\in[0,1]$ as shown in Fig. 6. A standard element can be mapped from the computational space (ξ,η,ζ) to an arbitrary tetrahedral element in the physical space (x,y,z) under the linear transformation $T:\Omega_e^{st}\mapsto\Omega_e$ defined by

$$\Upsilon = \{(\xi,\eta,\zeta)\,|\,0\le\xi\le 1; 0\le\eta\le 1-\xi; 0\le\zeta\le 1-\xi-\eta\}, \tag{3.6}$$

such as

$$\begin{aligned} x(\xi,\eta,\zeta) &= (1-\xi-\eta-\zeta)x_1+\xi x_2+\eta x_3+\zeta x_4, \\ y(\xi,\eta,\zeta) &= (1-\xi-\eta-\zeta)y_1+\xi y_2+\eta y_3+\zeta y_4, \\ z(\xi,\eta,\zeta) &= (1-\xi-\eta-\zeta)z_1+\xi z_2+\eta z_3+\zeta z_4. \end{aligned} \tag{3.7}$$

The Jacobian of this mapping is given by

$$\mathbf{J}=\left|\frac{\partial(x,y,z)}{\partial(\xi,\eta,\zeta)}\right|=\begin{vmatrix}\frac{\partial x}{\partial\xi} & \frac{\partial x}{\partial\eta} & \frac{\partial x}{\partial\zeta}\\ \frac{\partial y}{\partial\xi} & \frac{\partial y}{\partial\eta} & \frac{\partial y}{\partial\zeta}\\ \frac{\partial z}{\partial\xi} & \frac{\partial z}{\partial\eta} & \frac{\partial z}{\partial\zeta}\end{vmatrix}=\begin{vmatrix}x_2-x_1 & x_3-x_1 & x_4-x_1\\ y_2-y_1 & y_3-y_1 & y_4-y_1\\ z_2-z_1 & z_3-z_1 & z_4-z_1\end{vmatrix}=6|\mathbf{V}|, \tag{3.8}$$

where $|\mathbf{V}|$ is the volume of the real tetrahedral element in *xyz*-system.

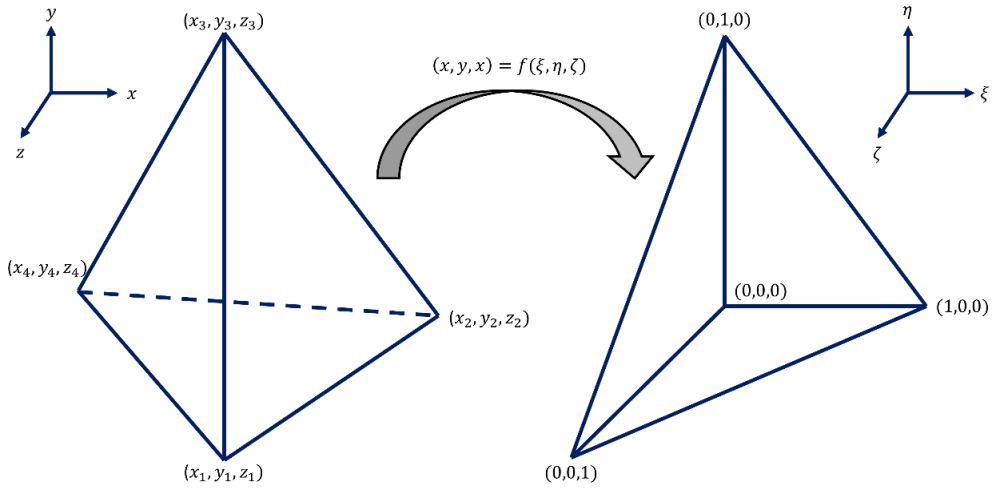

Fig. 6. Transformation from physical element to computational element in interval [0,1].

The DG discretization of the coupled system (3.1) is obtained by replacing the exact solutions with the corresponding approximation defined in Eq. (3.3) and multiplying by a test function $b_h \in \mathrm{V}_h(\mathcal{T}_h)$, and then integrating by parts over the element Ω_e. This results in the following weak formulation of the mixed system for $\mathbf{U}_h$ and Θ_h as,

$$\int_{\Omega_e}\Theta_h\, b_h\, dV+\int_{\Omega_e}\nabla b_h\cdot\mathbf{U}_h\, dV-\int_{\partial\Omega_e} b_h\mathbf{U}_h\cdot\mathbf{n}d\Gamma=0, \tag{3.9}$$

$$\frac{\partial}{\partial t}\int_{\Omega_e}\mathbf{U}_h\, b_h\, dV-\int_{\Omega_e}\nabla b_h\cdot\mathbf{F}^{inv}\, dV+\int_{\partial\Omega_e} b_h\mathbf{F}^{inv}\cdot\mathbf{n}d\Gamma-\int_{\Omega_e}\nabla b_h\cdot\mathbf{F}^{vis}\, dV+\int_{\partial\Omega_e} b_h\mathbf{F}^{vis}\cdot\mathbf{n}d\Gamma=0.$$

In this expression, **n** is the outward unit normal vector, V and Γ represent the volume and boundary of the element Ω_e, respectively. Since the numerical solutions $\mathbf{U}_h$ and Θ_h are discontinuous between element interfaces, the interface fluxes are not uniquely defined. The flux functions $\mathbf{U}_h \cdot \mathbf{n}$, $\mathbf{F}^{inv} \cdot \mathbf{n}$, and $\mathbf{F}^{vis} \cdot \mathbf{n}$ appearing in Eq. (3.9) are represented by numerical flux functions, namely single-valued functions defined at the cell interfaces. These fluxes typically depend on the discontinuous numerical solutions from both sides of the interface. The local reconstruction and normal at the edge interface of the field at two adjacent tetrahedral elements are illustrated in Fig 7.

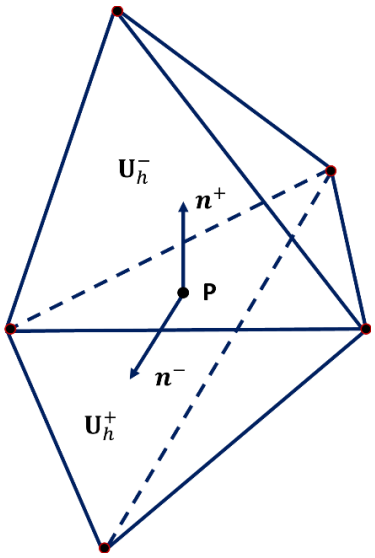

Fig. 7. Local reconstruction and normal at the edge interface of the field at two adjacent tetrahedral elements.

In this work, a dimensionless form of the local Lax-Friedrichs (LLF) flux is employed for inviscid terms. This monotone flux is commonly used in the DG method due to its computational cost efficiency. The LLF flux is also the most dissipative flux, which may improve the stability of the DG numerical approximation [15,16]. Its form can be written as,

$$\mathbf{F}^{inv} \cdot \mathbf{n} \approx \mathbf{H}^{inv}\left(\mathbf{U}_h^-, \mathbf{U}_h^+\right) = \frac{1}{2}\left[\mathbf{F}^{inv}\left(\mathbf{U}_h^-\right) + \mathbf{F}^{inv}\left(\mathbf{U}_h^+\right) - \alpha\left(\mathbf{U}_h^+ - \mathbf{U}_h^-\right)\right], \tag{3.10}$$

$$\alpha = \max\left(\left|\mathbf{U}_h^-\right| + a_s^-, \left|\mathbf{U}_h^+\right| + a_s^+\right).$$

Here, $a_s = \sqrt{T}/M$ is the speed of sound at an elemental interface, and the superscripts (+) and (–) denote the left and right states of the element interface. On the other hand, the BR1 flux [64] is used as the numerical fluxes to calculate the auxiliary and viscous fluxes at the elemental interfaces,

$$\begin{aligned}
&\mathbf{U}_h \cdot \mathbf{n} \approx \mathbf{H}^{aux}\left(\mathbf{U}_h^-, \mathbf{U}_h^+\right) = \frac{1}{2}\left[\mathbf{U}_h^- + \mathbf{U}_h^+\right], \\
&\mathbf{F}^{vis} \cdot \mathbf{n} \approx \mathbf{H}^{vis}\left(\mathbf{U}_h^-, \Theta_h^-, \mathbf{U}_h^+, \Theta_h^+\right) = \frac{1}{2}\left[\mathbf{F}^{vis}\left(\mathbf{U}_h^-, \Theta_h^-\right) + \mathbf{F}^{vis}\left(\mathbf{U}_h^+, \Theta_h^+\right)\right].
\end{aligned} \tag{3.11}$$

Then, the weak formulation of the mixed form (3.9) becomes

$$\begin{aligned}
&\int_{\Omega_e} \Theta_h\, b_h\, dV + \int_{\Omega_e} \nabla b_h \cdot \mathbf{U}_h\, dV - \int_{\partial\Omega_e} b_h \mathbf{H}^{aux}\, d\Gamma = 0, \\
&\frac{\partial}{\partial t}\int_{\Omega_e} \mathbf{U}_h\, b_h\, dV - \int_{\Omega_e} \nabla b_h \cdot \mathbf{F}^{inv}\, dV + \int_{\partial\Omega_e} b_h \mathbf{H}^{inv}\, d\Gamma - \int_{\Omega_e} \nabla b_h \cdot \mathbf{F}^{vis}\, dV + \int_{\partial\Omega_e} b_h \mathbf{H}^{vis}\, d\Gamma = 0.
\end{aligned} \tag{3.12}$$

All the integrals appearing in the elemental equations are calculated using the numerical quadrature rule with a few integration points consistent with the accuracy required. The volume and boundary integrals appearing in (3.12) are computed using the symmetric quadrature rule [85-87],

$$\begin{aligned}
&\int_{\Omega_e} f(x,y,z)\, dV = \mathbf{J}_V \cdot \int_{\Omega_{st}} f(\xi,\eta,\zeta)\, d\hat{V} = |\mathbf{V}| \sum_{j=1}^{N_q} w_j f\left(\xi_j^V, \eta_j^V, \zeta_j^V\right), \\
&\int_{\partial\Omega_e} g(x,y,z)\, d\Gamma = \mathbf{J}_S \cdot \int_{\partial\Omega_{st}} g(\xi,\eta,\zeta)\, d\hat{\Gamma} = |\mathbf{S}| \sum_{j=1}^{N_q} w_j g\left(\xi_j^S, \eta_j^S, \zeta_j^S\right).
\end{aligned} \tag{3.13}$$

In this expression, $\mathbf{J}_V, \mathbf{J}_S$ denote the Jacobian of the transformation for a tetrahedral and a triangle, respectively. $|\mathbf{V}|$ is the volume of the tetrahedral in physical space, $|\mathbf{S}|$ is the surface area of the triangle in physical space. $\xi_j^V, \eta_j^V, \zeta_j^V$ are the quadrature points on the reference tetrahedral, $\xi_j^S, \eta_j^S, \zeta_j^S$ are the quadrature points on the reference triangle, w_j is the weight associated with the quadrature points. N_q is the number of quadrature points for the reference element.

3.2 Temporal discretization

By assembling all the elemental contributions, the DG spatial discretization (3.12) leads to a system of semi-discrete ordinary differential equations in time for each element,

$$\frac{d\mathbf{U}_h}{dt} = \mathbf{M}^{-1}\mathbf{R}\left(\mathbf{U}_h\right). \tag{3.14}$$

Here, $\mathbf{M}$ is the elemental orthogonal mass matrix, and $\mathbf{R}\left(\mathbf{U}_h\right)$ is the residual vector of the system. In the present work, an explicit scheme is employed with high-order strong stability preserving (SSP) Runge-Kutta method, which preserves the monotonicity of the spatial discretization in any norm or semi-norm, coupled with first-order forward Euler time stepping [88]. The following third-order accurate SSP Runge-Kutta method proposed by Shu and Osher [89] is employed,

$$\begin{aligned}
\mathbf{U}_h^{(1)} &= \mathbf{U}_h^n + \Delta t\,\mathbf{M}^{-1}\mathbf{R}\left(\mathbf{U}_h\right) \\
\mathbf{U}_h^{(2)} &= \frac{3}{4}\mathbf{U}_h^n + \frac{1}{4}\mathbf{U}_h^{(1)} + \frac{1}{4}\Delta t\,\mathbf{M}^{-1}\mathbf{R}\left(\mathbf{U}_h^{(1)}\right) \\
\mathbf{U}_h^{n+1} &= \frac{1}{3}\mathbf{U}_h^n + \frac{2}{3}\mathbf{U}_h^{(2)} + \frac{2}{3}\Delta t\,\mathbf{M}^{-1}\mathbf{R}\left(\mathbf{U}_h^{(2)}\right).
\end{aligned} \tag{3.15}$$

The local time step Δt for each element is determined by the following relation

$$\Delta t = \frac{CFL}{\left(2k+1\right)} \frac{h}{\left|\lambda_{\text{inv}}^{\max}\right| + d\left|\lambda_{\text{vis}}^{\max}\right| \frac{2k+1}{h}}, \tag{3.16}$$

where *CFL* is the Courant-Friedrichs-Lewy number, *h* is the radius of the circumscribed sphere in the tetrahedral element Ω_e, and *d* is the dimension of the element. The $\lambda_{\text{inv}}^{\max}$ and $\lambda_{\text{vis}}^{\max}$ are the maximum wave speed of inviscid and viscous fluxes, respectively.

3.3 Maxwell velocity slip and Smoluchowski temperature jump boundary conditions

The velocity slip and temperature jump boundary conditions on the solid surface are necessary to accurately describe rarefied and microscale gas flows [1,5,84,90-92]. In 1879, Maxwell introduced a velocity slip boundary condition known as the Maxwell velocity slip condition [91]. In this boundary condition, the slip in tangential velocity near the solid surface $\mathbf{u}_{\text{slip}}$ is related to the tangential shear

stress $\mathbf{\Pi}_{\tan}$ and the tangential heat flux $\mathbf{Q}_{\tan}$. This slip condition can be expressed in the following form [13,84],

$$\mathbf{u}_{\text{slip}} - \mathbf{u}_{\text{wall}} = -\left(\frac{2-\sigma_v}{\sigma_v}\right)\frac{\lambda_{\text{mean}}}{\mu}\mathbf{\Pi}_{\tan} - \frac{3}{4}\frac{\Pr(\gamma-1)}{\gamma p}\mathbf{Q}_{\tan}, \tag{3.17}$$

where $\mathbf{u}_{\text{wall}}$ is the velocity vector of a solid surface, and λ_{mean} denotes the mean free path. We assume the solid surface is located at the origin of the normal coordinate. The tangential momentum accommodation coefficient is denoted by $\sigma_v\,(0 \le \sigma_v \le 1)$ which determines the proportion of the molecules reflected from the surface purely diffusely ($\sigma_v = 1$) or purely specular ($\sigma_v = 0$). The tangential shear stress and the tangential heat flux are defined in general coordinates at the surface,

$$\begin{aligned}\mathbf{\Pi}_{\tan} &= (\mathbf{n}\cdot\mathbf{\Pi})\cdot\mathbf{S},\\ \mathbf{Q}_{\tan} &= \mathbf{Q}\cdot\mathbf{S},\end{aligned} \tag{3.18}$$

where the **S**, defined as $\mathbf{S}=\mathbf{I}-\mathbf{n}\otimes\mathbf{n}$ using the dyadic product ($\otimes$), refers to the surface vector in which normal components are removed. If the constitutive relations of viscous stress and heat flux are taken as linear with the first-order accuracy, the slip condition (3.17) is simplified in cartesian coordinates into

$$u_{\text{slip}} - u_{\text{wall}} = \left(\frac{2-\sigma_v}{\sigma_v}\right)\lambda_{\text{mean}}\frac{\partial u}{\partial y} + \frac{3}{4}\frac{\Pr(\gamma-1)}{\gamma p}k\frac{\partial T}{\partial x}. \tag{3.19}$$

By analogy with the Maxwell velocity slip condition, the Smoluchowski jump boundary condition [92] can be written as

$$T_{\text{slip}} - T_{\text{wall}} = -\left(\frac{2-\sigma_T}{\sigma_T}\right)\frac{\lambda_{\text{mean}}}{k}\frac{2\gamma}{(\gamma+1)\Pr}\mathrm{Q}_{\text{normal}}. \tag{3.20}$$

Here T_{slip} is the gas temperature at the surface, T_{wall} is the temperature of the solid surface, and $\sigma_T\,(0 \le \sigma_T \le 1)$ denotes the thermal accommodation coefficient. If the constitutive relation of heat

flux is taken as linear with the first-order accuracy, the jump condition (3.20) is simplified in cartesian coordinates into

$$T_{\text{slip}} - T_{\text{wall}} = \left(\frac{2-\sigma_T}{\sigma_T} \right) \lambda_{\text{mean}} \frac{2\gamma}{(\gamma+1)\text{Pr}} \frac{\partial T}{\partial y}. \tag{3.21}$$

3.4 Langmuir velocity slip and temperature jump boundary conditions

Among the various slip and jump models, the so-called Langmuir slip model based on the physical adsorption isotherm may also be employed [9-11]. This boundary condition in mathematically Dirichlet form not only describes the slip and jump effects in the simplest way but also facilitates a hydrodynamic treatment of the entire density regime with a single formalism. This method takes the interfacial gas-surface molecule interaction into account. A fraction $\alpha\left(0 \le \alpha \le 1\right)$ of the molecules reaching thermal equilibrium with the solid wall can be expressed in dimensional form as [11]

$$\alpha = \begin{cases} \dfrac{\beta_{\text{slip}} p}{1+\beta_{\text{slip}} p}, & \text{for monatomic gas,} \\ \dfrac{\sqrt{\beta_{\text{slip}} p}}{1+\sqrt{\beta_{\text{slip}} p}}, & \text{for diatomic gas,} \end{cases} \tag{3.20}$$

where p is the surface pressure and the parameter β_{slip} depends on the wall temperature T_{wall} as well as interfacial interaction parameters. By considering the gas-surface molecular interaction process as a chemical reaction, the parameter β_{slip} can be expressed as

$$\beta_{\text{slip}} = \sqrt{\frac{\pi}{32}} \frac{\pi}{4c^2} \left(\frac{T_{\text{ref}}}{T_{\text{wall}}} \right)^{s+1/2} \exp\left(\frac{D_e}{k_B T_{\text{wall}}} \right) \frac{1}{p_{\text{ref}} \text{Kn}}, \tag{3.21}$$

where c is a gas constant of the exponent of the inverse power law of the particle interaction potential [10], p_{ref} and T_{ref} are reference pressure and temperature, Kn is the global Knudsen number, and D_e is the heat of adsorption, for example, $D_e = 5,255$ J/mol for the N_2-Al molecular interaction model.

The velocity slip and temperature jump boundary conditions in the Langmuir model are then determined simply based on the fraction α,

$$\begin{aligned}\mathbf{u} &= \alpha \mathbf{u}_{\text{wall}} + (1-\alpha)\mathbf{u}_{\text{gas}}, \\ T &= \alpha T_{\text{wall}} + (1-\alpha) T_{\text{gas}}.\end{aligned} \tag{3.22}$$

Here, $\mathbf{u}_{\text{gas}}, T_{\text{gas}}$ are the gas velocity vector and temperature, respectively, at the reference position—a mean free path away from the solid surface. Interestingly, with the definition $\alpha = 1/(1+4\sigma_v \text{Kn})$, a direct equivalence exists between the Maxwell and Langmuir models [11],

$$\frac{2-\sigma_v}{\sigma_v} = \sqrt{\frac{2}{\pi}} \frac{4c^2}{\pi} \left(\frac{T_{\text{wall}}}{T_{\text{ref}}} \right)^{1+1/(\nu-1)} \exp\left(-\frac{D_e}{k_B T_{\text{wall}}} \right). \tag{3.23}$$

3.5 Implementation of the positivity-preserving limiter

Numerical solutions in the DG scheme may lead to negative density and pressure during the time marching, even though the density and pressure should remain strictly positive physically [93,94]. Therefore, a positivity-preserving limiter is needed to enforce the positive density and pressure for every element and at every time. Zhang and Shu [95,96] proposed positivity-preserving limiters for the compressible Euler equations on two-dimensional rectangular and unstructured triangular meshes. The solution coefficients are limited in such a way that the positivity of density and pressure is performed locally at each element while the DG scheme remains conservative and its accuracy is maintained for smooth solutions. Here we developed a positivity-preserving limiter for conservation laws on three-dimensional unstructured tetrahedral meshes for the modal mixed DG formulation. The procedure for implementing the new limiter is summarized as follows.

To limit the density field at every tetrahedral element, we first define a small value $\omega = \min(10^{-13}, \bar{\rho}, \bar{p})$ based on the mean value of the computed density and pressure in the target cell. We then check the positivity of density by computing the minimum value of density, $\rho_{\min}$, after looping over the quadrature points in the local elements. Next, the limited coefficient θ_1 is evaluated from

$$\theta_1 = \min\left(\frac{\bar{\rho}-\omega}{\bar{\rho}-\rho_{\min}},1\right). \tag{3.24}$$

The high-order components of the density variable are then modified as

$$\mathbf{U}_h(\mathbf{x},t) = \hat{\mathrm{U}}_h^0(t)b_0(\mathbf{x}) + \theta_1\sum_{i=1}^{N_k}\hat{\mathrm{U}}_h^i(t)b_i(\mathbf{x}). \tag{3.25}$$

On the other hand, preserving the pressure at each local element requires the scaling of all high order moments of the solution of all conservative variables with the second limited coefficient θ_2. To compute θ_2, it is necessary to solve the quadratic equation,

$$p\left[(1-t)\bar{\mathbf{W}}+t\bar{\mathbf{U}}\right] = \omega, \quad 0\le t\le 1, \tag{3.26}$$

where $\bar{\mathbf{W}}$ is the mean solution and $\bar{\mathbf{U}}$ is the limited density solution in conservative variables. The limited coefficient θ_2 can be determined by selecting the minimum value of *t* among all the quadrature points. The high order components of the conservative variables are then modified as

$$\mathbf{U}_h(\mathbf{x},t) = \hat{\mathrm{U}}_h^0(t)b_0(\mathbf{x}) + \theta_2\sum_{i=1}^{N_k}\hat{\mathrm{U}}_h^i(t)b_i(\mathbf{x}), \tag{3.27}$$

4 Results and discussion: flow and thermal analysis of rarefied and microscale monatomic and diatomic gases in thermal non-equilibrium

4.1. Verification of the present DG scheme

4.1.1. Accuracy test

To verify the order of accuracy of the DG scheme, we consider a smooth density wave propagation problem with an analytical solution. The initial condition for the density propagation is given by,

$$\left.\begin{aligned} u(x,0) &= 1.0 \\ \rho(x,0) &= 1.0 + 0.2\sin(\pi x) \\ p(x,0) &= 1.0 \end{aligned}\right\} \quad \forall x \in [0,6], \tag{4.1}$$

with the periodic boundary condition on both sides of the domain. The analytical solution of this problem is given by,

$$\left.\begin{aligned} u(x,t) &= 1.0 \\ \rho(x,t) &= 1.0 + 0.2\sin(\pi(x-t)) \\ p(x,t) &= 1.0 \end{aligned}\right\}. \tag{4.2}$$

The accuracy of the DG scheme is examined based on the density distribution for different orders (P^k , k being the polynomial order) up to piecewise cubic (P^3) fourth-order, as shown in Fig. 8. A large deviation from the analytical solution is observed in case of the first-order piecewise constant (P^0) polynomial. The numerical errors and the order of accuracy are also evaluated based on the density solution. The results are very close to the computational results of Qiu *et al*. [97]. Overall, the results confirm that the present DG scheme achieves the desired order of accuracy (k + 1) in this unsteady problem. The piecewise linear (P^1) second-order accuracy was applied throughout all following computations.

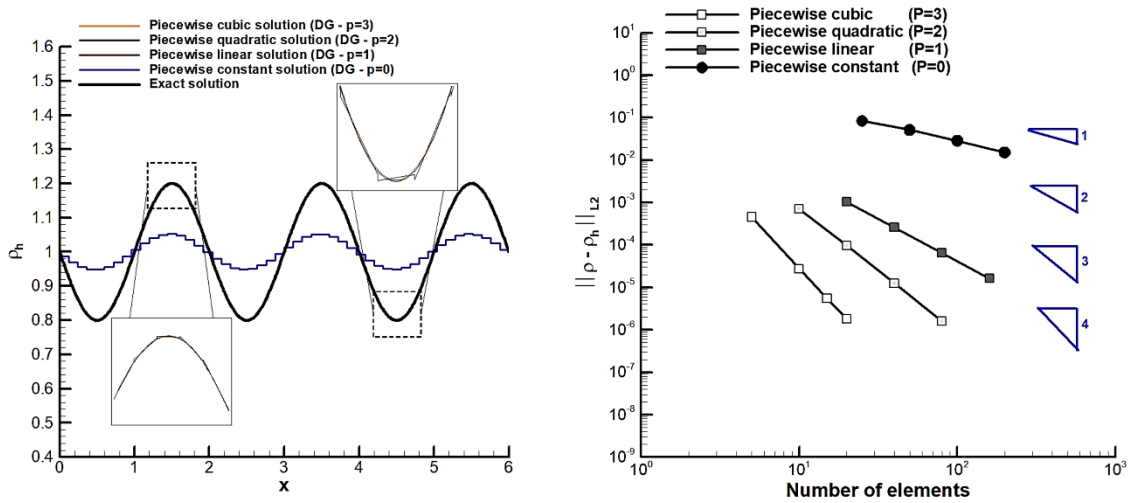

Fig. 8. Accuracy test: comparison of solution profiles and Euclidean norm of density in the smooth density wave propagation problem.

4.1.2. Three-dimensional supersonic flow over a forward-facing step

To further verify the present DG scheme of the zeroth-order constitutive model, we compute a three-dimensional supersonic inviscid flow over a forward-facing step. This problem, originally studied by Woodward and Colella [98], is a benchmark problem for testing high-resolution shock-capturing schemes. The computational domain defined by $[0,3]\times[0,1]\times[0,0.05]$ was constructed using unstructured tetrahedral elements with mesh size $h=0.01$. The forward-facing step is located at $x=0.6$ with height 0.2 inside the tunnel. Initially, a right-moving uniform supersonic flow with M = 3 is imposed in the whole computational domain. Flow variables with $\rho=1, u=3, v=w=0, p=1$ are imposed as the initial conditions. Reflective boundary conditions are applied on the upper and along the walls of the tunnel. Inflow and outflow boundary conditions are imposed at the entrance and the exit, respectively. The symmetry boundary condition is applied for the z-direction. A geometric singularity at the corner of the step is resolved with the same second-order accuracy. Figure 9 shows the Mach contours obtained with the zeroth-order constitutive model at t =2.85 sec. The results indicate that the present DG scheme of the zeroth-order constitutive model captures important flow features very well, especially the physical instability and roll up of the contact line.

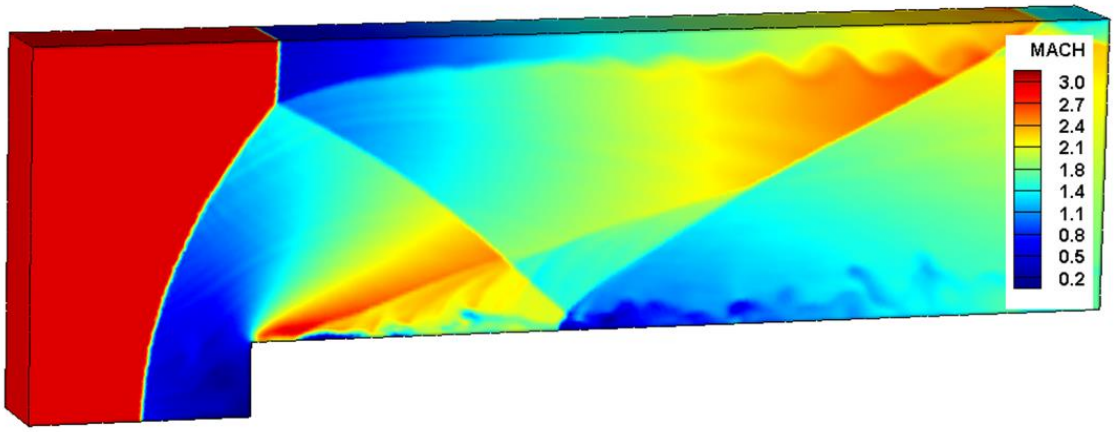

Fig. 9. Three-dimensional supersonic flow over forward-facing step: computed Mach contours obtained with the zeroth-order constitutive model at M =3, Kn = 6.22×10^{-8} and t = 2.85 sec.

4.2. One-dimensional stationary viscous inner structure of hypersonic shock waves

To validate the present DG scheme in the first- and second-order constitutive models, we consider a one-dimensional viscous inner structure of hypersonic shock waves [8-10,15,20,34,39,99-107]. A shock structure with strong gradients is regarded as one of the fundamental problems in the kinetic

theory and thermodynamics of gases, and has been studied by many theoreticians and experimentalists over several decades. For example, it has a big impact on the overall flow patterns around hypersonic aerospace vehicles at high altitude. Although the shock structure problem does not involve any solid wall boundary, the calculation of the shock inner structure presents severe theoretical and computational challenges, because of its inherent nonlinearity in the formation of the shock wave through self-steepening, and subtle interplay with the viscous dissipation. For instance, the high order hydrodynamic approach beyond the first-order NSF theory based on the original Grad's moment method failed to yield shock solutions beyond a relatively small value of Mach number, around 1.65 [100].

The stationary shock wave structure problem is defined as a very thin (on the order of the mean free path, equivalently, a Knudsen number close to 1.0) stationary gas flow region between the supersonic upstream and subsonic downstream. When the freestream Mach number is 10, the degree of thermal nonequilibrium defined as $\sqrt{2/\gamma\pi}\cdot \mathrm{Kn}\cdot M$ reaches as high as 6.74, leading to a very high nonequilibrium flow in which the viscous effect is dominant over the hydrostatic pressure. The upstream and downstream states are determined by the so-called Rankine-Hugoniot condition derived from the conservation laws with the zeroth-order constitutive model. To compare the inner structure of shock waves, the shock density thickness is considered one of the key measures to best characterize the essence of profiles of the shock inner structure, and to assess the accuracy of the computational models.

Figure 10 summarizes the overall comparison of the inverse shock density thickness of the first- and second-order constitutive models and experimental results [104-107] for argon and nitrogen gases. The verification of a modal DG scheme of the first-order NSF constitutive model was already conducted in a previous study [15] using a full analytical NSF solution in closed elementary functional form for the case of Pr=3/4 and a Maxwellian molecule [103]. In the present study, we focus on validating the second-order constitutive models of a diatomic gas. It was shown in Fig. 10 that values of the inverse shock density thickness for the second-order model are in excellent agreement with the experimental data. Moreover, the second-order constitutive model captured very well the inverse shock density thickness for all Mach numbers, up to 10. Note that the first-order constitutive model yields an inverse shock density thickness much larger than the experimental data.

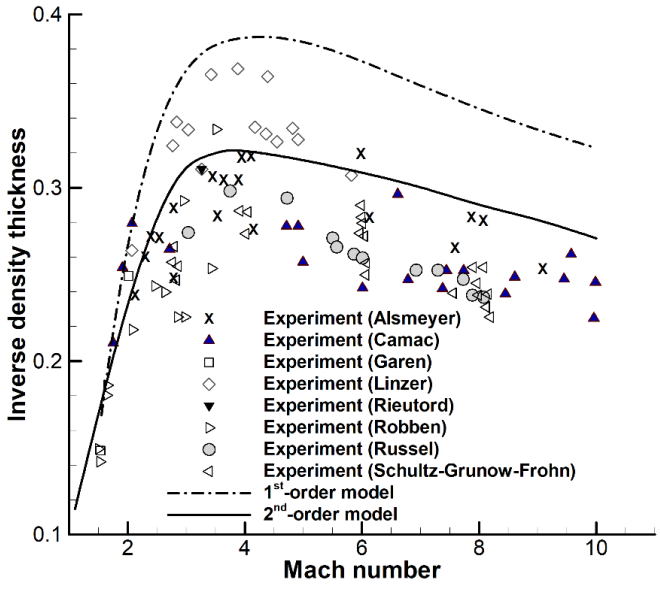

(a)

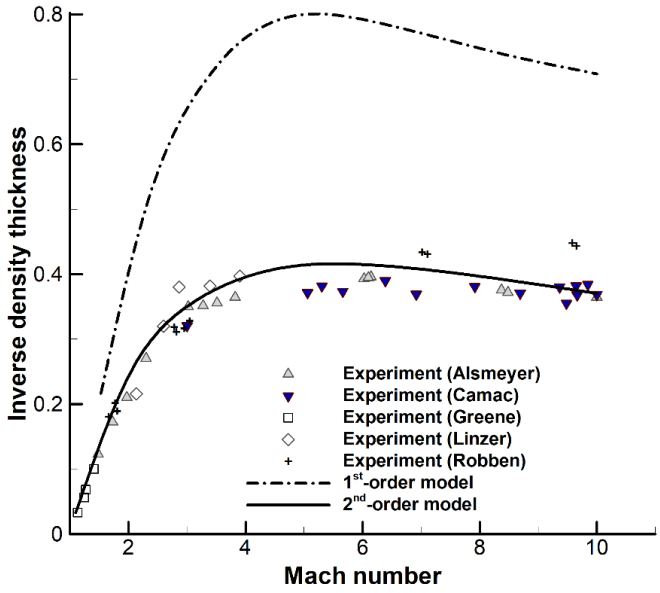

(b)

Fig. 10. One-dimensional shock viscous inner structure problem: inverse density thickness for (a) argon, and (b) nitrogen gas (Reproduced with permission from Singh *et al*., "Topology of the second-order constitutive model based on the Boltzmann–Curtiss kinetic equation for diatomic and polyatomic gases," Phys. Fluids 32, 026104 (2020). Copyright 2020 AIP).

Figure 11 compares profiles of the shock inner structure —the normalized density and non-conservative variables, stress and heat flux—in nitrogen gas for two Mach numbers, 2.0 and 6.1, with the experimental data. It shows that the difference between the first-order results and experimental data becomes noticeable for high Mach number flows, while the second-order results are much closer to the experimental data. On the other hand, Fig. 12 illustrates the difference between monatomic and diatomic

gases in the viscous inner structure of shock waves at M = 6.1. The effect of the diatomic gas is more visible in the viscous stress and heat flux profiles.

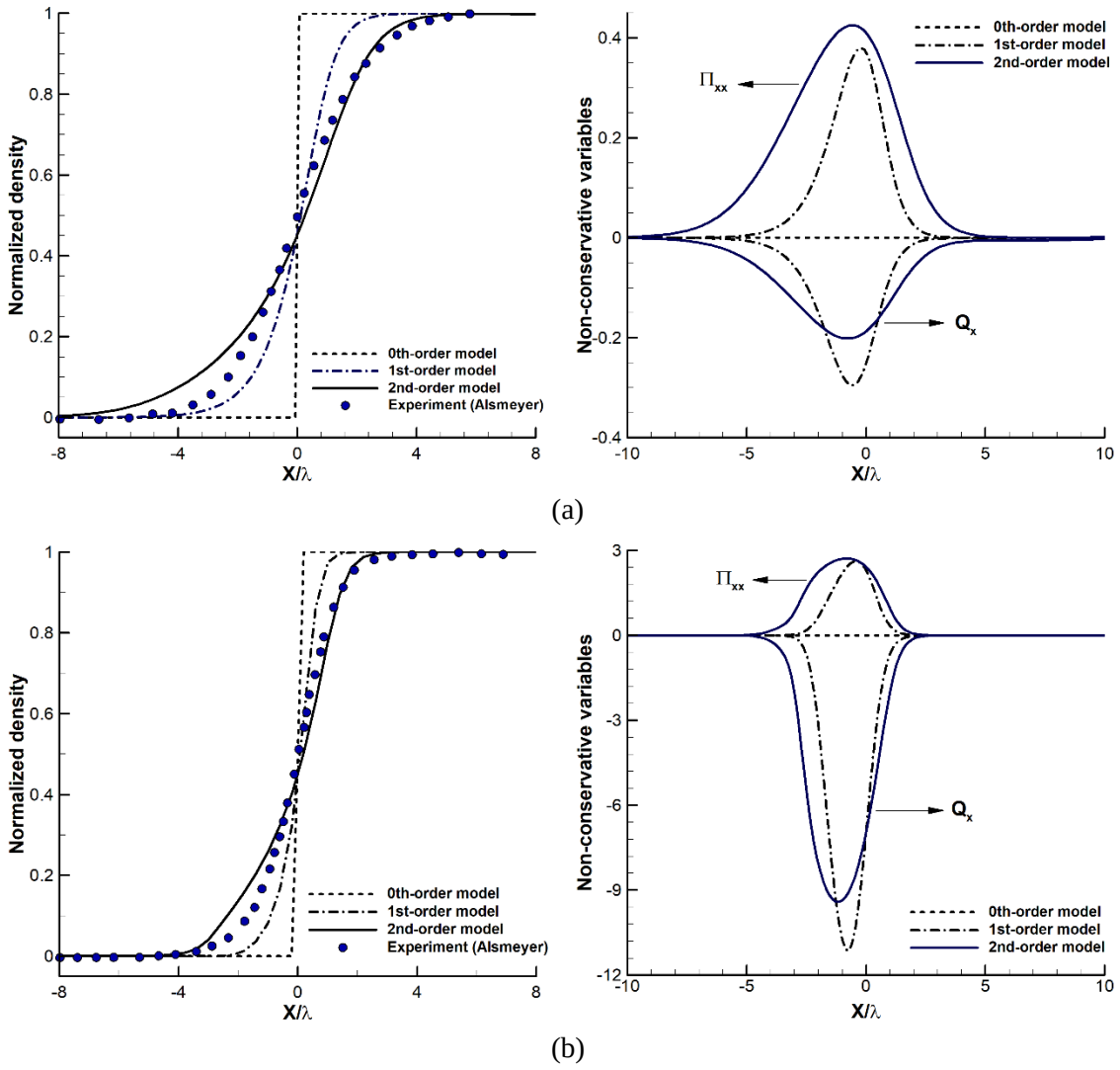

Fig. 11. One-dimensional shock viscous inner structure problem: comparison of normalized density and non-conservative variables solutions with the zeroth-, first- and second-order constitutive models and experiment result [104] for nitrogen gas at (a) M = 2.0, and (b) M = 6.1.

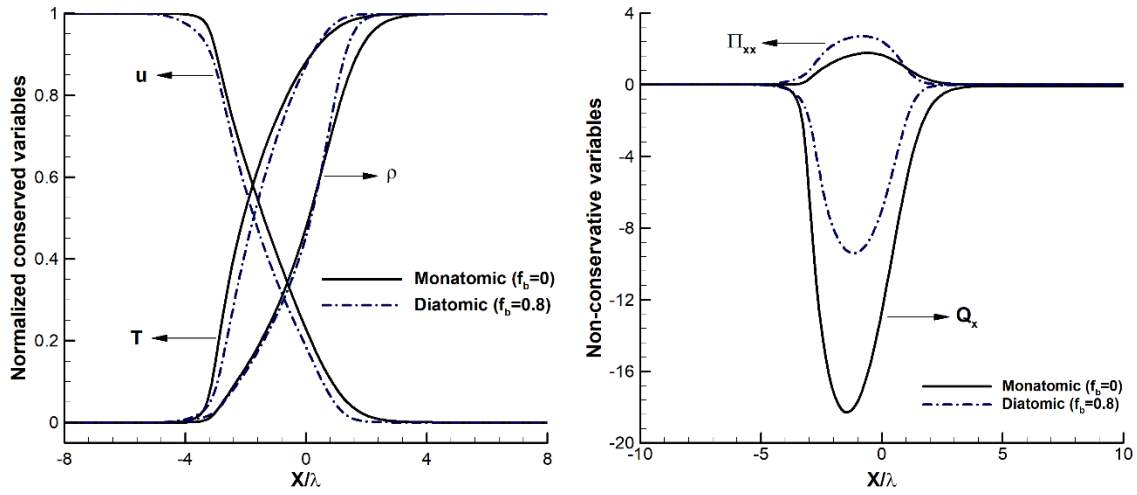

Fig. 12. One-dimensional shock viscous inner structure problem: effects of monatomic and diatomic gases on normalized conservative and non-conservative variables solutions obtained with the second-order constitutive model at M = 6.1.

4.3. Two-dimensional subsonic and hypersonic gas flows past a cylinder

In the next benchmark problem, we consider a two-dimensional subsonic flow past a cylinder at M = 0.1 and Re =40, which was studied experimentally in [108]. Here, the Reynolds number is defined based on the diameter of the cylinder. The outer boundary of the computational domain is set to be approximately 15 times the cylinder diameter away from the cylinder surface. For all two-dimensional stationary wall cases considered in the present study, the Maxwell-Smoluchowski boundary conditions are applied with momentum and thermal accommodation coefficients, $\sigma_v = 0.8$, $\sigma_T = 0.75$. At Re= 40, flow is laminar and two large stable wakes appear behind the cylinder. Figure 13 compares the streamlines computed by the second-order model and those obtained by experiment. Stationary separation bubbles can be clearly identified in both plots, and the size of the separation region is predicted accurately compared with experimental data.

Further, we consider a two-dimensional hypersonic rarefied flow past a cylinder at M =5.48 for argon gas, from the continuum regime (Kn=0.0002) to the slip regime (Kn=0.02) and then to the transition regime (Kn = 0.2, 0.5). Because of its geometrical simplicity, it is the most-studied benchmark problem in rarefied and microscale gas flows. Figure 14 summarizes the overall comparison of the Mach contours of the zeroth-, first-, and second-order constitutive models and the DSMC at four different Knudsen numbers, 0.002, 0.02, 0.2, and 0.5. The Mach contours illustrate that the flow fields

vary significantly as the Knudsen number increases from 0.0002 to 0.5. When the Knudsen number is very low, i.e., Kn = 0.0002, the discrepancies between the zeroth-, first- and second-order constitutive models and the DSMC results are negligible, as shown in Fig. 14(a). When the Knudsen number increases to Kn=0.02 in the slip regime, a noticeable difference appears near the bow shock waves, especially between the first- and second-order constitutive models, as shown in Fig. 14(b). Finally, when the Knudsen number increases to Kn=0.2, 0.5 in the transition regime, significant differences are present all over the flow fields in this high thermal nonequilibrium case ($\sqrt{2/\gamma\pi}\cdot \mathrm{Kn}\cdot M$ =0.68, 1.69), as shown in Figs. 14(c), (d). A most notable difference is found in the structure of the stand-off shock wave in the frontal parts: a thicker and broader shock structure in the second-order model as compared with the first-order model. Overall, the second-order model shows better agreement on average with the DSMC method than the first-order model, even though there are some deviations along the stagnation line.

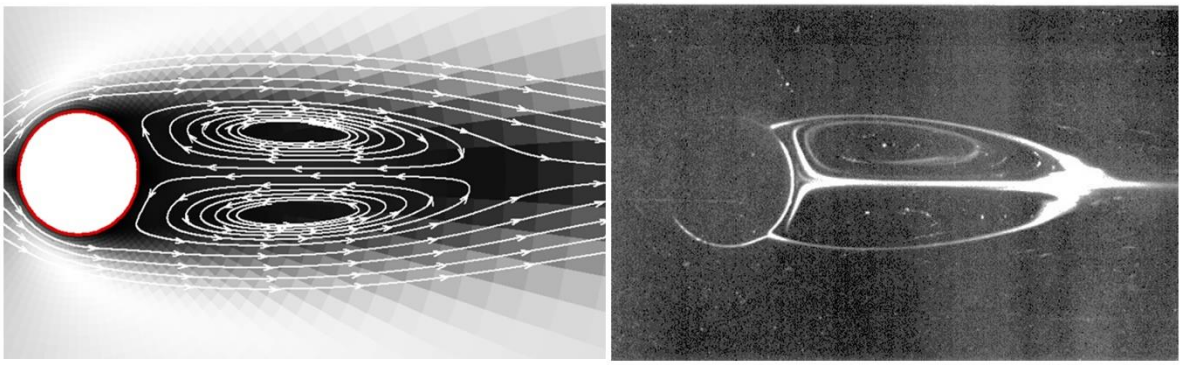

Fig. 13. Two-dimensional subsonic flow past a cylinder: comparison of streamlines of the flow field solution obtained with the second-order constitutive model and experimental result [108] at M =0.1 and Re = 40.

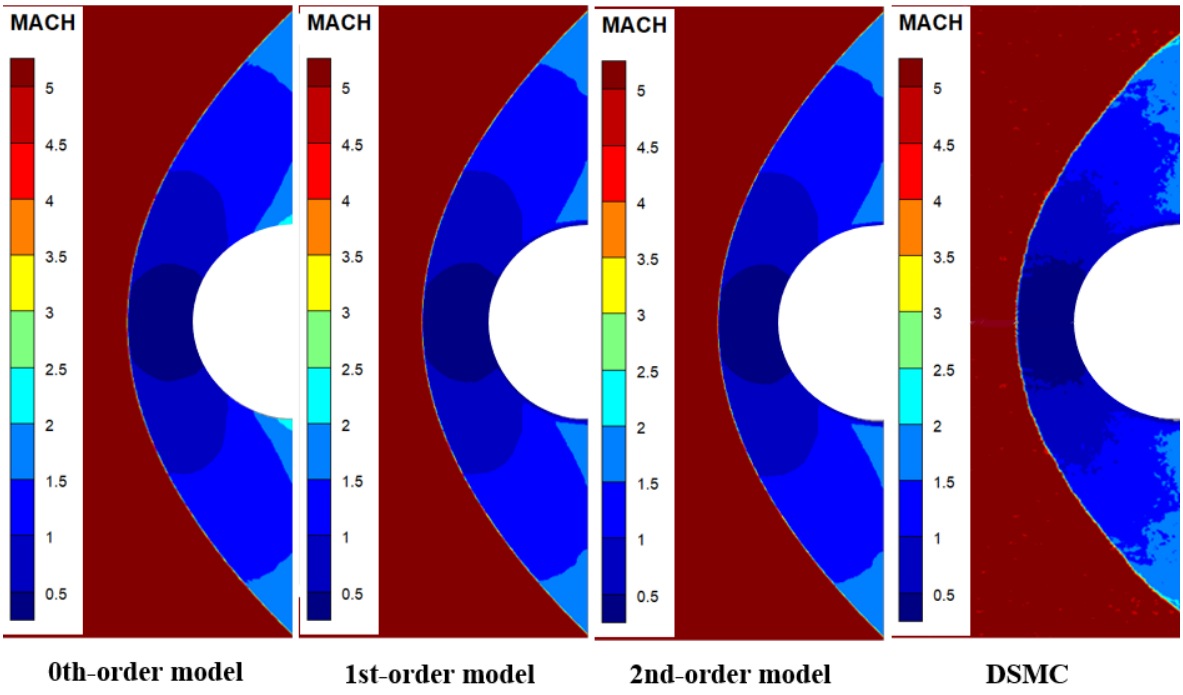

(a) Kn=0.0002

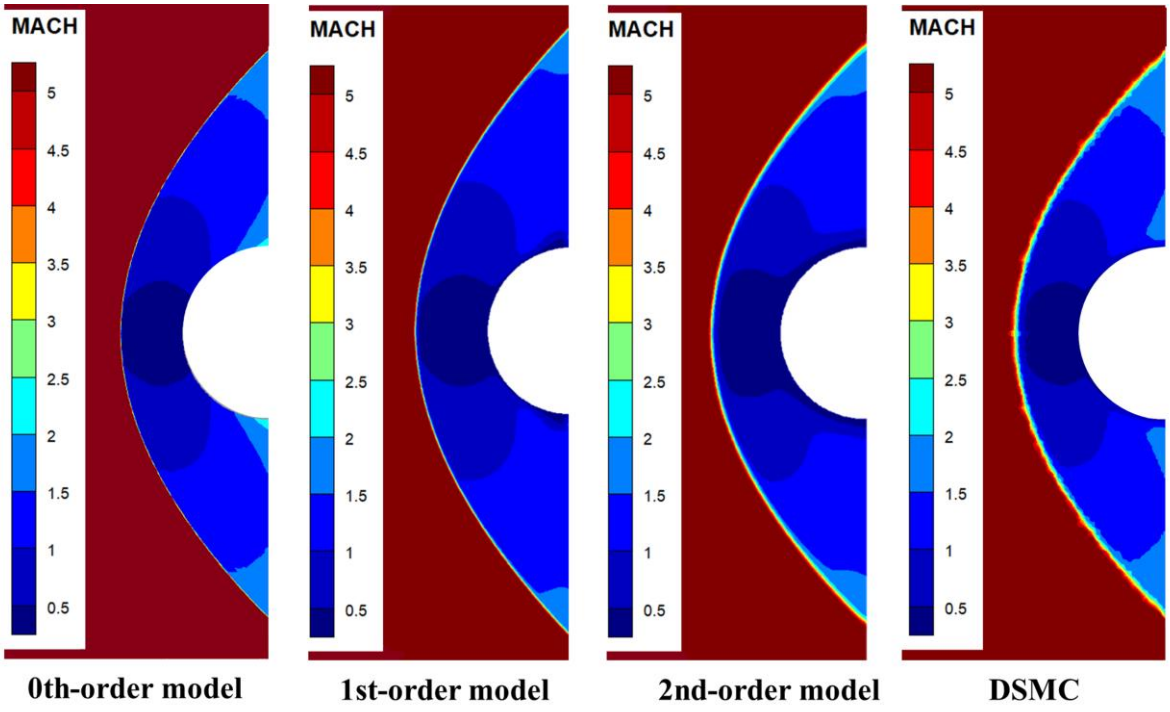

(b) Kn=0.02

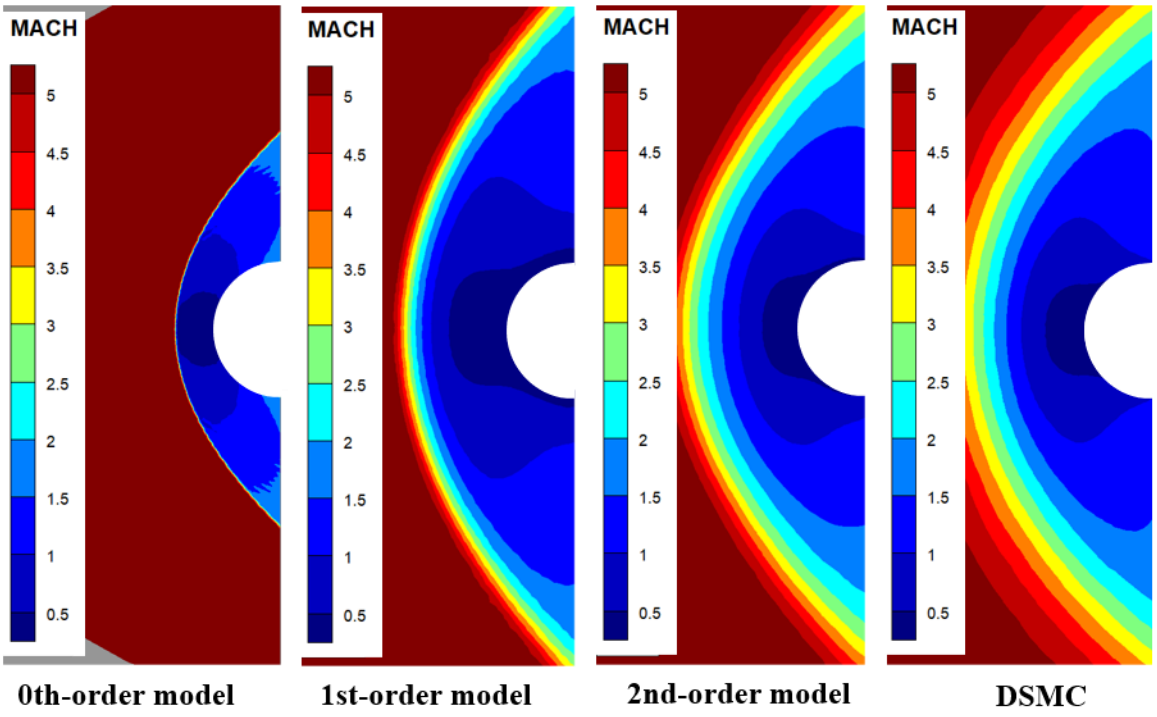

(c) Kn=0.2

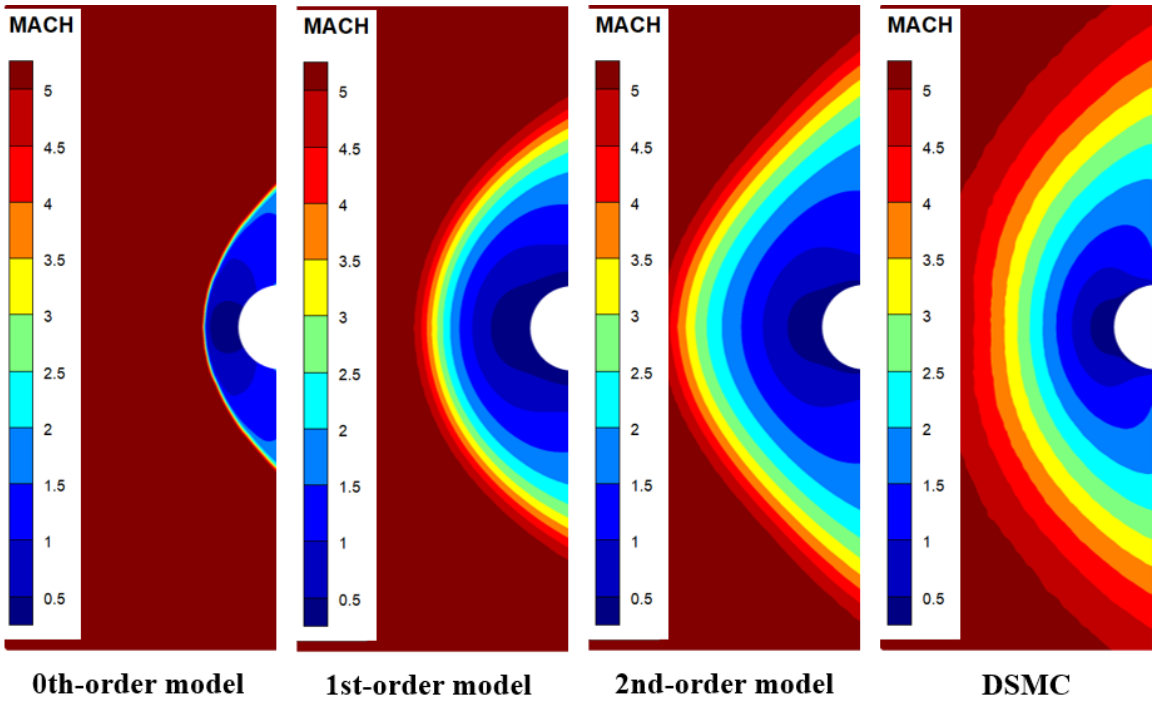

(d) Kn=0.5

Fig. 14. Two-dimensional hypersonic flow past a cylinder: comparison of Mach contours obtained with the zeroth-, first- and second-order constitutive models and DSMC result for argon gas at M = 5.48 with Kn = 0.0002, 0.02, 0.2, and 0.5.

We also investigate a two-dimensional hypersonic flow past a cylinder at M =12, Kn =0.0118 for nitrogen gas. The freestream density and temperature are assumed to be $\rho_\infty = 7.48\times10^{-5}\ \mathrm{kg/m^3}$ and $T_\infty = 217.45\ \mathrm{K}$. An isothermal boundary condition with temperature $T_w = 1000\ \mathrm{K}$ was imposed on the cylinder wall. In this high Mach number flow with high wall temperature, the downstream of the bow shock waves may undergo some degree of vibrational excitations due to the high temperature. However, for direct comparison with the previous DSMC study [109] in which energy transfer to vibrational modes is neglected, the second-order constitutive model without the vibrational mode is used in the present work. We hope to extend the present DG method to the recently developed Boltzmann-Curtiss-based second-order constitutive model including the vibrational mode [39] in the future.

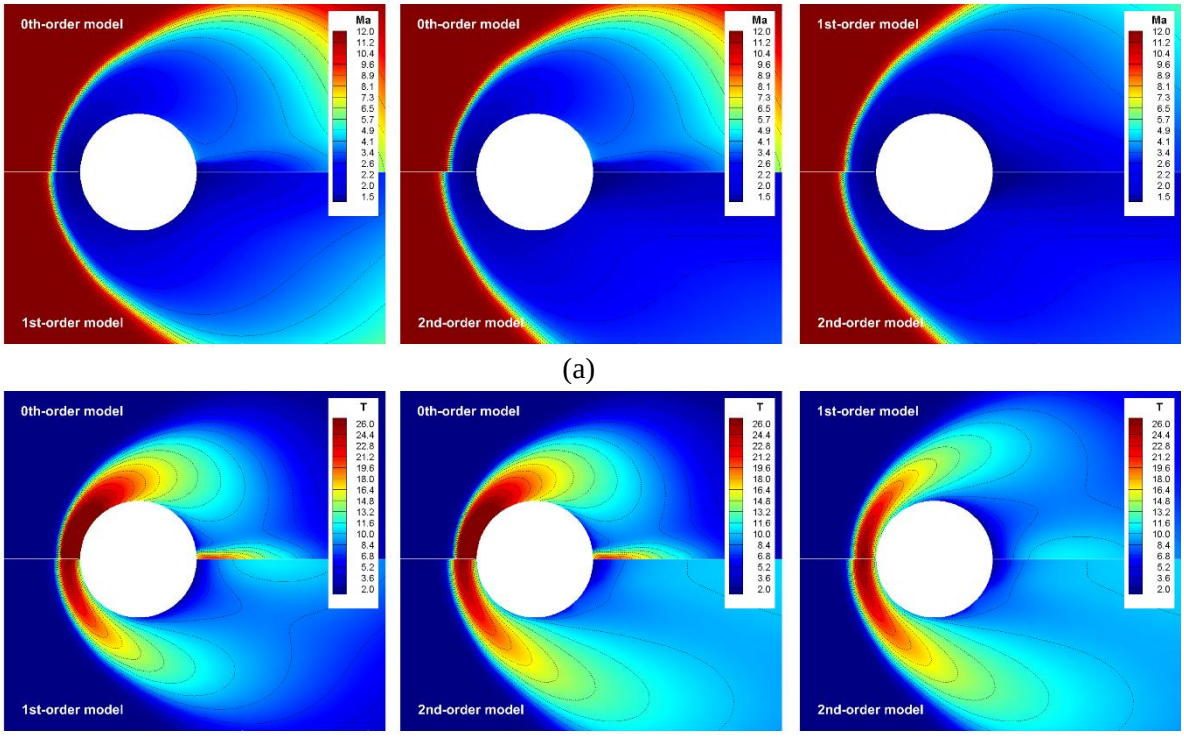

Fig. 15. Two-dimensional hypersonic flow past a cylinder: comparison of (a) Mach, and (b) temperature contours obtained with the zeroth-, first- and second-order constitutive models for nitrogen gas at M = 12 and Kn = 0.0118.

Figure 15 compares the Mach and temperature contours calculated by the zeroth-, first- and second-order constitutive models. It can be noted that the shock stand-off distance increases with the increasing

order of constitutive model. Figure 16 compares the normalized heat flux coefficient at the cylinder wall obtained using the first- and second-order constitutive models, and the DSMC [109]. The second-order constitutive model predicts the surface heat flux in the frontal parts of cylinder in better agreement with the DSMC than the first-order constitutive model.

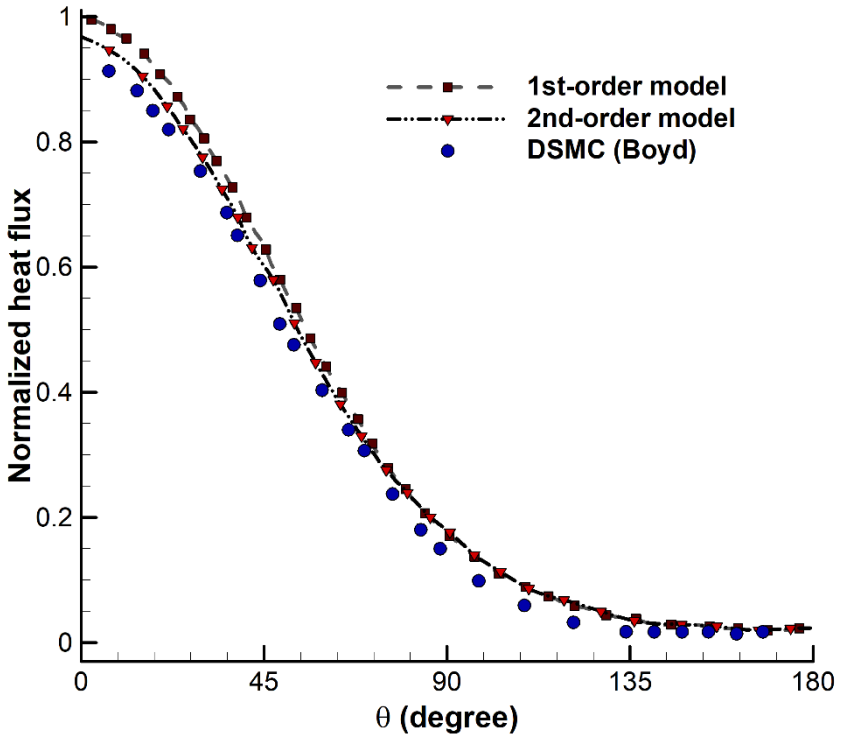

Fig. 16. Two-dimensional hypersonic flow past a cylinder: comparison of normalized heat flux coefficients obtained with the first- and second-order constitutive models, and DSMC result [109] for nitrogen gas at M = 12 and Kn = 0.0118.

4.4. Two-dimensional microscale internal cylindrical Couette flow with a moving wall

We also consider a moving wall problem to investigate the physical Knudsen layer in subsonic microscale flow: a two-dimensional internal cylindrical Couette flow with moving wall [110-115]. The flow and wall boundary conditions for this benchmark case are set according to the DSMC study by Tibbs *et al*. [110]—Knudsen number (0.5), initial temperature of argon gas and cylinder walls (273 K), and the ratio of outer and inner cylinder radius (5/3). The inner cylinder is assumed to be rotating with a constant Mach number of 0.3, while the outer cylinder is held stationary. The flow domain is discretized by uniform grids with 120 grid cells along the radial direction, which is considered fine enough to reduce numerical error [113]. For this moving wall problem, the Maxwell-Smoluchowski

boundary conditions are applied with the momentum and thermal accommodation coefficients $\sigma_v = 1.0,\ \sigma_T = 0.98$.

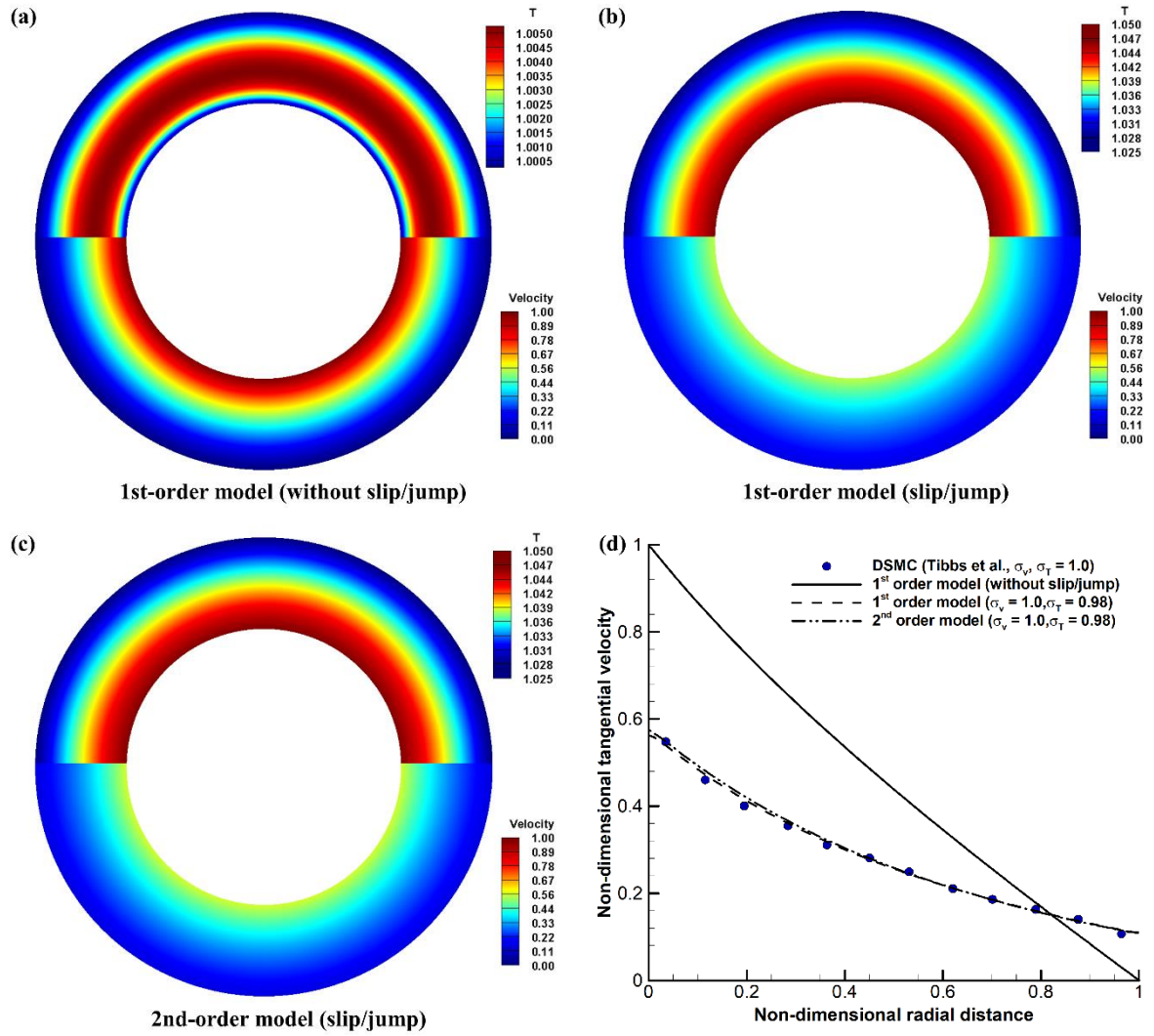

Fig. 17. Two-dimensional microscale internal cylindrical Couette flow with moving wall: temperature and velocity contours obtained with (a) first-order model without slip/jump, (b) first-order model with slip/jump, (c) second-order model with slip/jump, and (d) comparison of normalized tangential velocity obtained using the first- and second- order constitutive models with DSMC results [110] measured along the radial direction at M = 0.3, Kn =0.5 and $\sigma_v = 1.0,\ \sigma_T = 0.98$.

Figures 17(a)-(c) illustrate temperature and velocity contours computed by the first-order constitutive model without and with the slip and jump conditions, and the second-order constitutive

model with the slip and jump conditions. Figure 17(d) compares the tangential velocity distribution in the radial direction obtained by the first-and second-order constitutive models and the DSMC. The results show that both the first- and second-order constitutive models with slip and jump conditions predict the velocity profile in close agreement with the DSMC. On the other hand, the velocity profile predicted with the first-order constitutive model without slip and jump conditions significantly deviates from the DSMC data, showing the critical role of the slip and jump conditions in the microscale flow.

4.5. Three-dimensional subsonic and hypersonic gas flows past a sphere

As another benchmark problem, we study a subsonic flow past a sphere [116,117] at a freestream Mach number (0.3) and for two different Reynolds numbers (37.7, 133). The adiabatic thermal condition is imposed on the wall. The Maxwell-Smoluchowski boundary conditions are applied with the momentum and thermal accommodation coefficient $\sigma_v = 0.9$, $\sigma_T = 0.85$ for all three-dimensional cases considered in the present study. The computational domain was discretized with 98,000 tetrahedral elements with 25,344 grid points.

Figure 18 compares the streamlines computed by the second-order model and those obtained by experiment [116]. As is the case with a two-dimensional subsonic flow past a cylinder, stationary separation bubbles are clearly identified in both plots. Moreover, the size of the separation region is predicted accurately compared with experimental data for both Reynolds numbers.

Figure 19 compares the distribution of the skin friction coefficient at the surface of the sphere for the first- and second-order constitutive models, and Wang's numerical study [117]. The coefficient is computed at the cross section (y=0) of the sphere. As expected from the small deviation from thermal equilibrium ($\gamma M^2 / \mathrm{Re}$ =0.001) in the present flow, the difference between the first-order and second-order models is shown to be negligible.

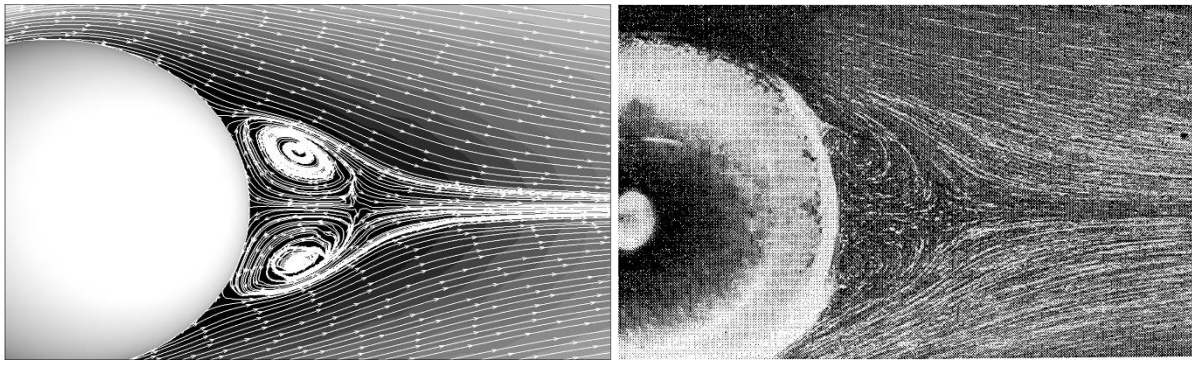

(a) Re = 37.7

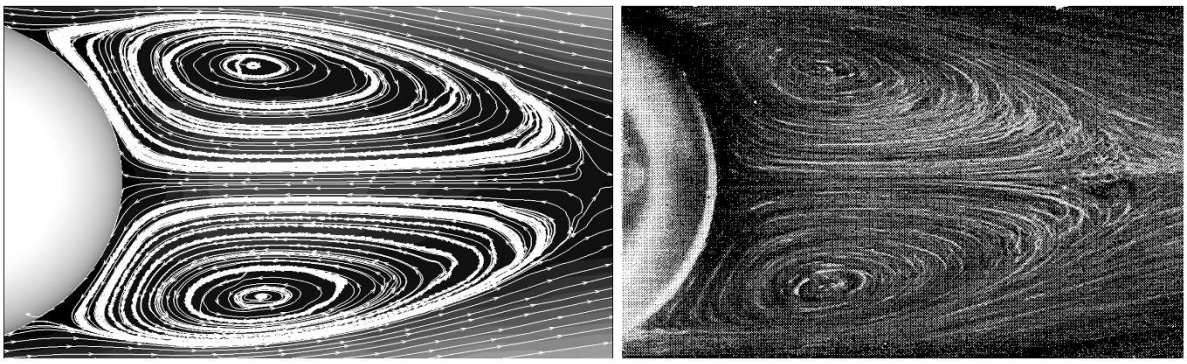

(b) Re = 133

Fig. 18. Three-dimensional subsonic flow past a sphere: comparison of streamlines of the flow field obtained with the second-order constitutive model and experimental result [116] at M=0.3 with (a) Re =37.7 and (b) Re =133.

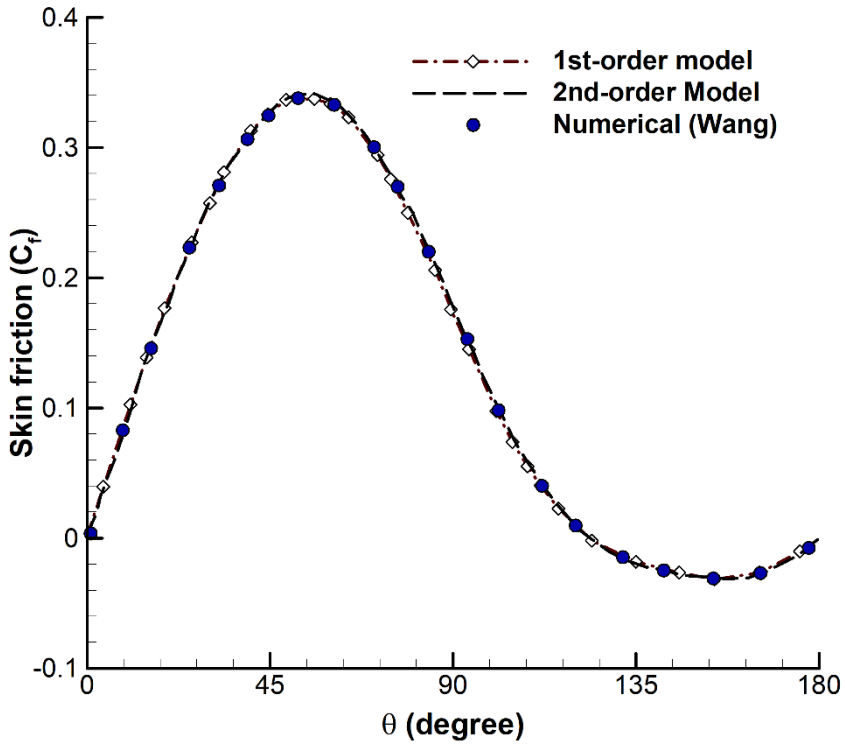

Fig. 19. Three-dimensional subsonic flow past a sphere: comparison of computed skin friction coefficient obtained with the first- and second-order constitutive models, and Wang's numerical data [117] at M =0.3 and Re = 118.

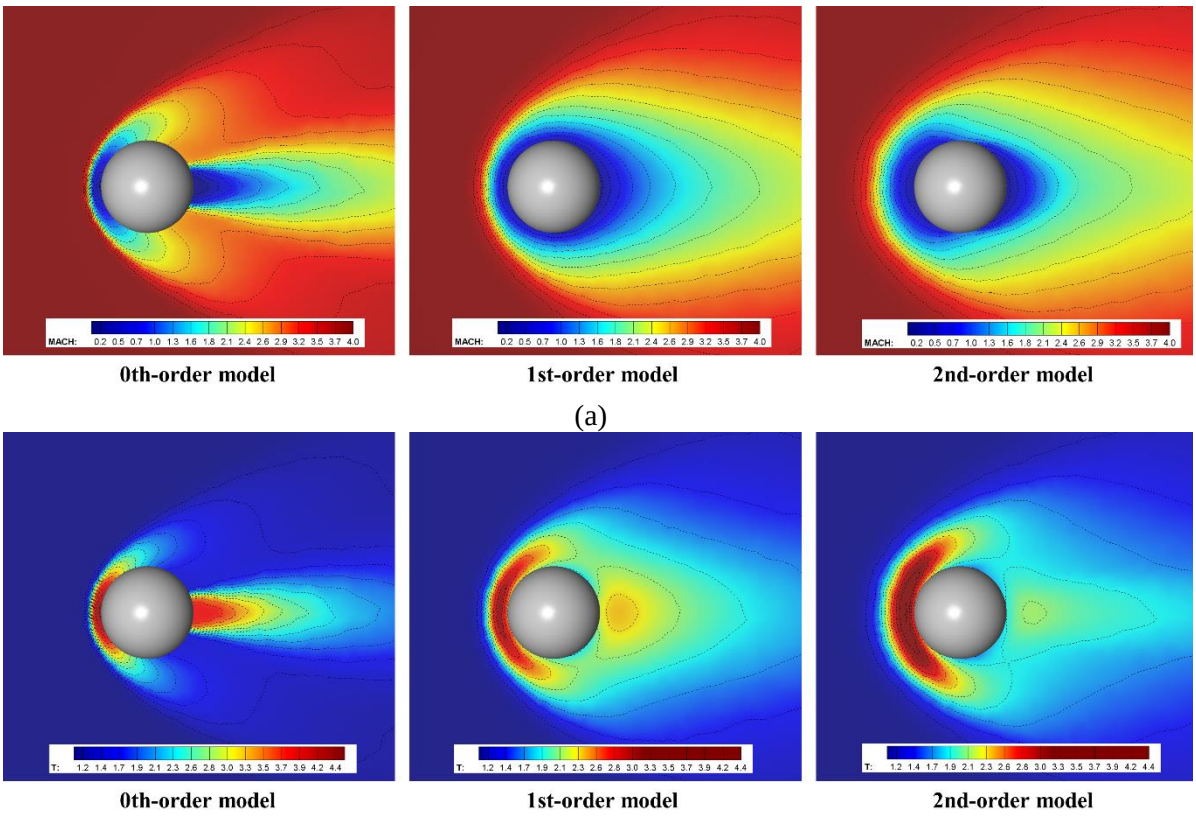

Fig. 20. Three-dimensional supersonic flow past a sphere: (a) Mach, and (b) temperature contours obtained with the zeroth-, first- and second-order constitutive models for nitrogen gas at M =4.0 and Kn =0.01.

We also study a hypersonic flow past a sphere with M =4.0 and Kn=0.01. The working gas is assumed to be nitrogen gas with $f_b = 0.8$. Figure 20 compares the Mach and temperature contours calculated by the zeroth-, first-, and second-order constitutive models. In contrast with the subsonic case, there is substantial difference in the thermal solutions of the first-order and the second-order models since the degree of thermal nonequilibrium ($\sqrt{2/\gamma\pi}\cdot \mathrm{Kn}\cdot M$ =0.027) in the present case is not negligible.

4.6. Three-dimensional hypersonic gas flow past a flat plate

As the second three-dimensional benchmark problem, we consider a hypersonic flow past a flat plate with zero pressure gradient at the freestream conditions, M =4.37 and Kn = 0.0013. Here, the

Knudsen number is defined based on the length of the plate. This problem is intended to assess the accuracy of the present DG scheme for a moderate Reynolds number flow ($\sqrt{\gamma\pi/2}\cdot M/\mathrm{Kn}$ =5,439). The temperature and pressure of freestream argon gas are assumed to be 300 K and 4.14×10^7 Pa, respectively. The surface temperature of the flat plate is considered to be 500 K. The computational domain contains 428,053 tetrahedral elements and 80,058 grid points.

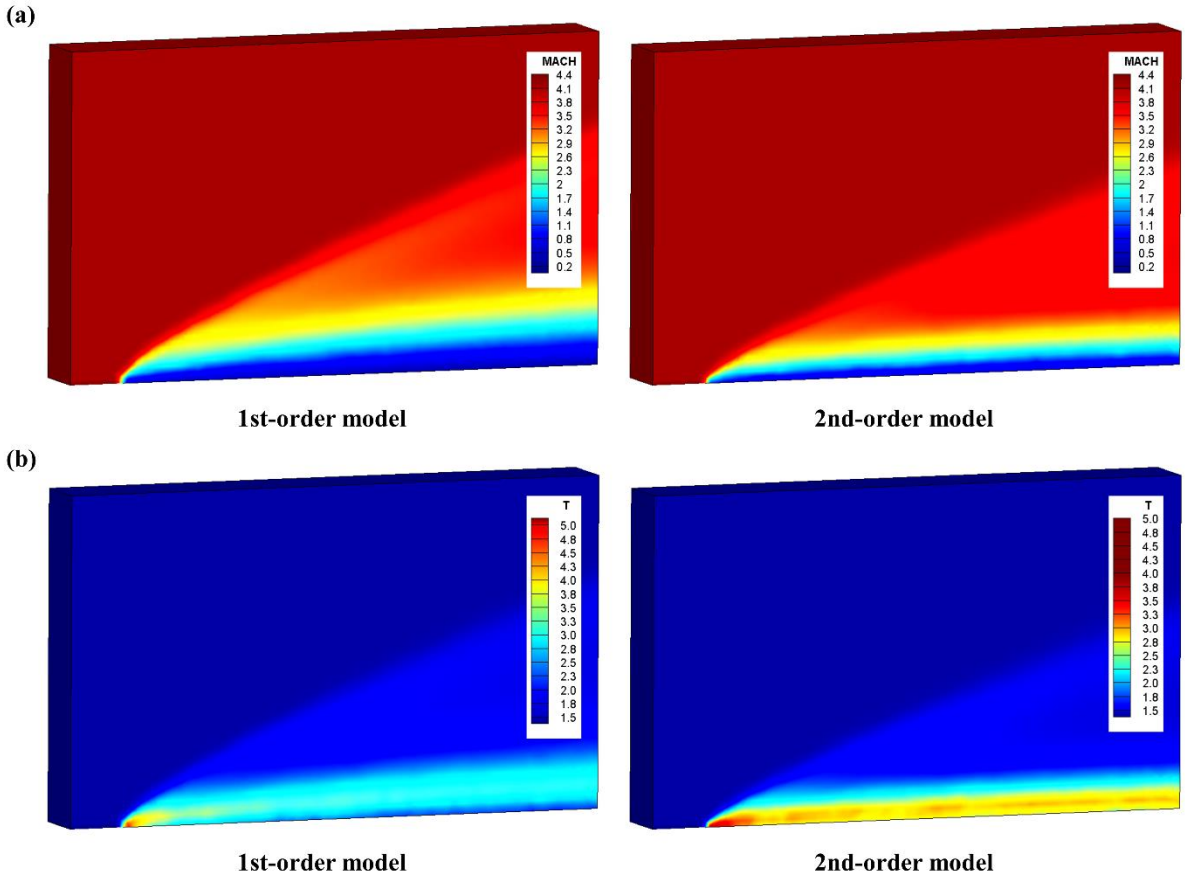

Fig. 21. Three-dimensional supersonic flow past a flat plate: (a) Mach, and (b) temperature contours obtained with the first- and second-order constitutive models for argon gas at M=4.37 and Kn=0.0013.

Figure 21 presents the Mach and temperature contours computed by the first-order and second-order constitutive models in a three-dimensional laminar flow over the flat plate. It is observed that the second-order constitutive model predicts a thinner wall boundary layer and higher temperature distribution near the wall than the first-order constitutive model. Figure 22 compares the velocity slip at the flat plate surface predicted by the first-order constitutive model without and with the slip and

jump conditions, the second-order constitutive model with the slip and jump conditions, and the DSMC [2]. The solution of the second-order constitutive model is found to be in better agreement with the DSMC solution than the solution of the first-order constitutive model.

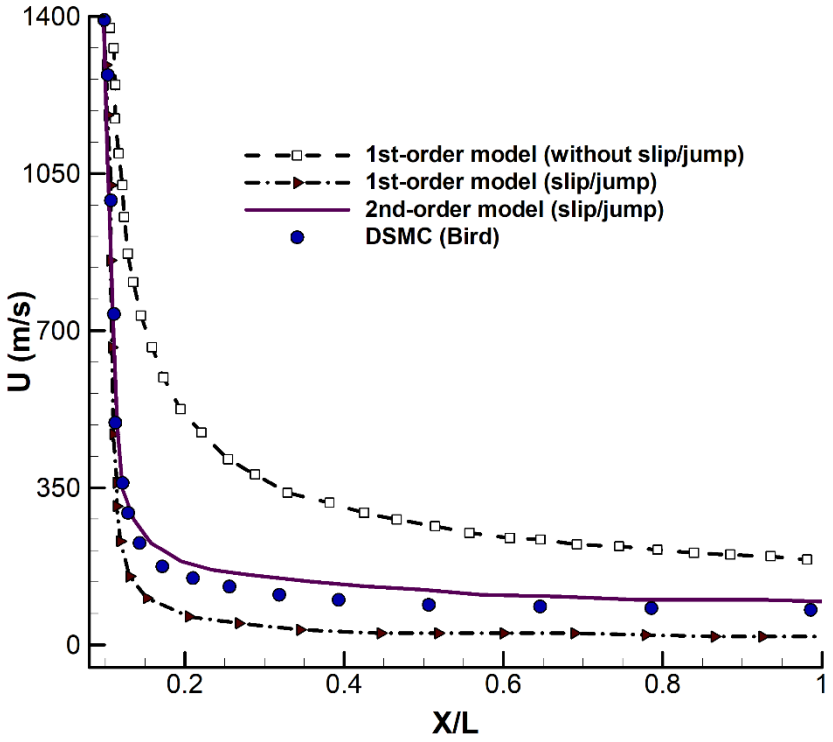

Fig. 22. Three-dimensional supersonic flow past a flat plate: comparison of computed gas velocity at flat plate surface obtained with first- and second-order constitutive models, and DSMC result [2] for argon gas at *M*=4.37 and Kn=0.0013.

4.7. Three-dimensional hypersonic flow past a suborbital re-entry vehicle

Finally, to assess the performance of the present second-order constitutive model for handling a complex three-dimensional configuration problem, we investigate a hypersonic gas flow past a suborbital re-entry vehicle, the intermediate experimental vehicle (IXV) of the European Space Agency (ESA). The freestream condition of nitrogen gas with $f_b = 0.8$ is set as M =5.0, Kn = 0.02, $T_\infty = 300K$. The angle of attack of the vehicle is assumed to be 15 degrees. A constant temperature condition with $T_w = 500K$ is imposed on the wall surface. The computational domain is defined by the total of 676,187 tetrahedral elements and 72,522 triangle elements on the wall surface.

Figure 23 compares the contours of Mach, temperature, velocity magnitude and streamlines, and degree of non-equilibrium calculated using the first- and second-order constitutive models. There are two distinctive regions of compression and expansion in the frontal and rear parts of the re-entry vehicle, respectively. In the present case with a non-negligible degree of thermal nonequilibrium in the freestream ($\sqrt{2/\gamma\pi}\cdot \mathrm{Kn}\cdot M$ =0.067), there is a substantial difference between the first- and second-order constitutive models in the flow fields. The nonequilibrium effects begin to show up near the stand-off shock wave region on the frontal part of the vehicle, where strong compression occurs. The second-order constitutive model predicts a thicker bow shock structure in the frontal part of the vehicle than the first-order constitutive model, resulting in a weaker compression inside the shock wave. In addition, the nonequilibrium effects show up in the wake region in the rear part of the vehicle where rapid expansion occurs.

Figure 23(c) shows the contours of velocity magnitude and a few representative streamlines, which provide more detailed information about what the gas particles experience—for example, acceleration or deceleration—and how differently the first-order and second-order constitutive models describe them. Based on the Rayleigh-Onsager dissipation function [79], the degree of thermal non-equilibrium $\hat{R}$ defined in Eq. (2.20) plays a vital role in the theory of irreversible thermodynamics and is directly related to entropy production in non-equilibrium processes. In Figure 23(d), the contours of $\hat{R}$ are shown to identify what regions are expected to deviate significantly from the near-local-equilibrium assumption. The degree of thermal nonequilibrium is high in the bow shock region where the flow experiences sudden changes. Moreover, the flow experiences very strong expansion at the rear part of re-entry vehicle, producing the most visible non-equilibrium, as high as $\hat{R}=20$. In general, the first-order constitutive model over-estimates the degree of-non-equilibrium, which can be considered the ultimate reason for its poor performance for high Knudsen and Mach number flows. Besides these findings, the present results demonstrate that numerical simulation of the second-order constitutive model is possible for hypersonic rarefied flows over three-dimensional re-entry vehicles with complicated configurations.

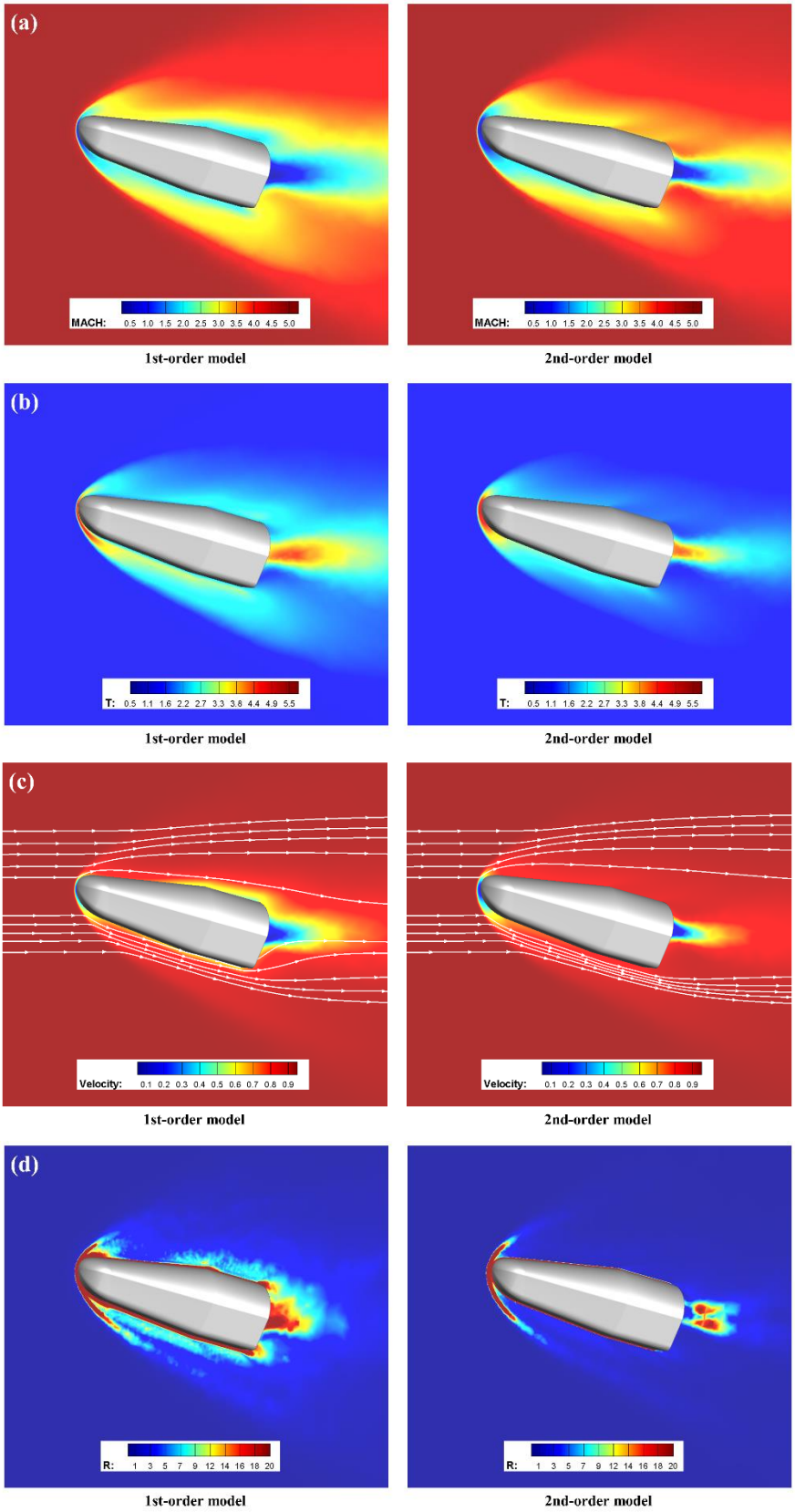

Fig. 23. Three-dimensional hypersonic flow past a suborbital re-entry vehicle: contours of (a) Mach, (b) temperature, (c) velocity magnitude and streamlines, and (d) degree of non-equilibrium obtained with the first- and second-order constitutive models for nitrogen gas at M=5.0, Kn=0.02 and angle of attack 15 degrees.

4.8. Computing time of the three-dimensional modal DG solver

Numerical computations of the flow problems studied so far indicated that the computing time of the three-dimensional DG code of the second-order constitutive model is comparable to that of the first-order NSF code. The only excess load, which is caused by the addition of few iterations (less than 10 in most cases) when the viscous stresses and heat fluxes are calculated from the implicit algebraic constitutive equations for given thermodynamic forces, occupies a small fraction of computing time in the code (less than 40%). Computational simulations on hypersonic gas flows (M=4, Kn=0.01) past a sphere with 64,868 cells were conducted on Intel Xeon workstation using a single processor. The total run times in this three-dimensional problem for the two methods (the first-order NSF and the second-order constitutive models) were found to be 12.5 and 17 hours, respectively, resulting in a 35% increase compared with the run time of NSF code.

5 Concluding remarks

We developed a three-dimensional mixed modal discontinuous Galerkin (DG) method based on tetrahedral meshes for simulating all flow regimes, from subsonic to hypersonic rarefied and microscale gas flows, within a single framework. In the mixed modal DG scheme, auxiliary variables were introduced to solve the implicit nonlinear coupled constitutive relations of non-conserved variables which describe diatomic and polyatomic gases in strong thermal nonequilibrium.

The second-order constitutive model was derived from the Boltzmann–Curtiss kinetic equation for diatomic and polyatomic molecules with a moment of inertia and an angular momentum. During the derivation, two tenets—the closing-last balanced closure and the cumulant expansion based on the canonical distribution function in the exponential form—were applied to the moment equations of the Boltzmann–Curtiss kinetic equation. To solve the multi-dimensional second-order constitutive model, we developed a decomposition algorithm based on the compression-expansion and velocity shear sub-problems. The decomposition method developed initially for handling surface integrals in the two-dimensional FVM framework was extended for handling both surface and volume integrals in the three-

dimensional DG framework. An iterative computational algorithm was also presented for numerical solutions of the multi-dimensional second-order constitutive relations.

In the DG scheme, we used the hierarchical basis functions based on orthogonal Jacobi polynomials for tetrahedral elements. The symmetric quadrature rule was adopted for evaluating surface and volume integration. The LLF and the BR1 scheme were used for handling the inviscid and viscous flux functions, respectively. For temporal discretization, we employed an explicit third-order accurate SSP-RK scheme that preserves the monotonicity of the spatial discretization in norm or semi-norm coupled with the first-order forward Euler time stepping. To enforce positive density and pressure during the time marching, we developed a positivity-preserving limiter for conservation laws on three-dimensional unstructured tetrahedral meshes. The Maxwell-Smoluchowski and Langmuir velocity slip and temperature jump boundary conditions were implemented into the multi-dimensional DG framework.

Using the present DG scheme, we investigated various gas flows in one-, two-, and three-dimensional space. To verify the order of accuracy of the numerical scheme, we first solved a smooth density wave propagation problem. We then solved a three-dimensional supersonic forward-step facing step problem to test the inviscid solver in the present DG scheme. To assess the ability of the new computational models to capture physical phenomena, we investigated several gas flows in a wide range of continuum-rarefied and microscale regimes: the inner structure of one-dimensional shock waves, subsonic and hypersonic flows past a cylinder and a sphere, a cylindrical Couette flow with a moving wall, hypersonic flows over a flat plate, and a hypersonic flow around a suborbital IXV re-entry vehicle.

The second-order constitutive model includes the conventional first-order constitutive model as a subset and therefore its solution recovers the solution of the first-order constitutive model in the continuum regime. However, as the degree of thermal nonequilibrium increases, the discrepancy in the numerical solutions grows and the first-order constitutive model is no longer considered valid: for instance, for the viscous inner structure of shock waves. Overall, the computational results in rarefied and microscale flow regimes showed that the second-order constitutive model yields solutions that are in better agreement with the DSMC and experimental data.

This study focused on the second-order constitutive models of translational and rotational non-equilibrium within the hydrodynamic framework. To cover all rarefied and microscale flow regimes at high temperature, from ground to the boundary of earth's atmosphere, it will be essential to include vibrational and chemical non-equilibrium effects. We hope to report the results of our study of these problems in the future.

Acknowledgements

R.S.M. acknowledges the support from the National Research Foundation of Korea funded by the Ministry of Science and ICT (NRF 2017-R1A2B2007634 and NRF 2017-R1A5A1015311), South Korea. S.S. acknowledges the partial support provided by the Nanyang Technological University Singapore, through the NAP-SUG grant.

References

[1] J.M. Reese, M.A. Gallis, D.A. Lockerby, New directions in fluid dynamics: Non-equilibrium aerodynamic and microsystem flows, Philos. Trans. R. Soc. A 361 (2003) 2967–2988.

[2] G.A. Bird, Molecular Gas Dynamics and the Direct Simulation of Gas Flows, Oxford University Press, Oxford, 1994.

[3] R.S. Myong, A. Karchani, O. Ejtehadi, A review and perspective on a convergence analysis of the direct simulation Monte Carlo and solution verification, Phys. Fluids. 31 (2019) 066101.

[4] H. Grad, On the kinetic theory of rarefied gases, Commun. Pure Appl. Math. 2 (1949) 331–407.

[5] H.S. Tsien, Superaerodynamics, mechanics of rarefied gases, J. Aeronaut Sci. 13 (1946) 653–664.

[6] B.C. Eu, Kinetic Theory and Irreversible Thermodynamics, Wiley, New York, 1992.

[7] B.C. Eu, A modified moment method and irreversible thermodynamics, J. Chem. Phys. 73 (1980) 2958.

[8] R.S. Myong, Thermodynamically consistent hydrodynamic computational models for high-Knudsen-number gas flows, Phys. Fluids. 11 (1999) 2788–2802.

[9] R.S. Myong, A computational method for Eu's generalized hydrodynamic equations of rarefied and microscale gasdynamics, J. Comput. Phys. 168 (2001) 47–72.

[10] R.S. Myong, A generalized hydrodynamic computational model for rarefied and microscale diatomic gas flows, J. Comput. Phys. 195 (2004) 655–676.

[11] R.S. Myong, Gaseous slip model based on the Langmuir adsorption isotherm, Phys. Fluids. 16 (2004) 104–117.

[12] R.S. Myong, A full analytical solution for the force-driven compressible Poiseuille gas flow based on a nonlinear coupled constitutive relation, Phys. Fluids 23 (2011) 012002.

[13] R.S. Myong, Theoretical description of the gaseous Knudsen layer in Couette flow based on the second-order constitutive and slip-jump models, Phys. Fluids. 28 (2016) 012002.

[14] J.W. Ahn, C. Kim, An axisymmetric computational model of generalized hydrodynamic theory for rarefied multi-species gas flows, J. Comput. Phys. 228 (2009) 4088–4117.

[15] N.T.P. Le, H. Xiao, R.S. Myong, A triangular discontinuous Galerkin method for non-Newtonian implicit constitutive models of rarefied and microscale gases, J. Comput. Phys. 273 (2014) 160–184.

[16] L.P. Raj, S. Singh, A. Karchani, R.S. Myong, A super-parallel mixed explicit discontinuous Galerkin method for the second-order Boltzmann-based constitutive models of rarefied and microscale gases, Comput. Fluids. 157 (2017) 146–163.

[17] R.S. Myong, Numerical simulation of hypersonic rarefied flows using the second-order constitutive model of the Boltzmann equation, in: Advances in Some Hypersonic Vehicles Technologies, InTech, 2018.

[18] H. Xiao, Q.J. He, Aero-heating in hypersonic continuum and rarefied gas flows, Aerosp. Sci. Technol. 82-83 (2018) 566.

[19] Z. Jiang, W. Zhao, Z. Yuan, W. Chen, R.S. Myong, Computation of hypersonic flows over flying configurations using a nonlinear constitutive model, AIAA J. 57 (2019) 5252.

[20] Z. Jiang, W. Zhao, W. Chen, R.K. Agarwal, Computation of shock wave structure using a simpler set of generalized hydrodynamic equations based on nonlinear coupled constitutive relations, Shock Waves 29 (2019) 1227.

[21] Z. Jiang, W. Zhao, W. Chen, R.K. Agarwal, An undecomposed hybrid algorithm for nonlinear coupled constitutive relations of rarefied gas dynamics, Commun. Comput. Phys. 26(3) (2019) 880.

[22] Z. Yuan, W. Zhao, Z. Jiang, W. Chen, Numerical simulation of hypersonic reaction flows with nonlinear coupled constitutive relations, Aerosp. Sci. Technol. 112 (2021) 106591.

[23] C.L.M.H. Navier, Mémoire sur les lois du Mouvement des Fluides, Mem. Acad. Sci. Inst. France 6 (1823) 389–440.

[24] G.G. Stokes, On the Theories of the Internal Friction of Fluids in Motion and of the Equilibrium and Motion of Elastic Solids, Trans. Cambridge Philos. Soc. 8 (1845) 287–319.

[25] G. Emanuel, Bulk viscosity of a dilute polyatomic gas, Phys. Fluids A 2 (1990) 2252–2254.

[26] G. Emanuel, Bulk viscosity in the Navier-Stokes equations, Int. J. Eng. Sc. 36 (1998) 1313.

[27] N. Carlevaro, G. Montani, Bulk viscosity effects on the early universe stability, Mod. Phys. Lett. A 20 (2005) 1729–1739.

[28] M.S. Cramer, Numerical estimates for the bulk viscosity of ideal gases, Phys. Fluids 24 (2012) 066102.

[29] Y. Zhu, C. Zhang, X. Chen, H. Yuan, J. Wu, S. Chen, C. Lee, M. Gad-El-Hak, Transition in hypersonic boundary layers: Role of dilatational waves, AIAA J. 54 (2016) 3039–3049.

[30] S. Pan, E. Johnsen, The role of bulk viscosity on the decay of compressible, homogeneous, isotropic turbulence, J. Fluid Mech. 833 (2017) 717–744.

[31] F. Bahmani, M.S. Cramer, Suppression of shock-induced separation in fluids having large bulk viscosities, J. Fluid Mech. 756 (2014)

[32] S. Singh, R.S. Myong, A computational study of bulk viscosity effects on shock-vortex interaction using discontinuous Galerkin method, J. Comput. Fluids Eng. 22 (2017) 86–95.

[33] S. Singh, A. Karchani, R.S. Myong, Non-equilibrium effects of diatomic and polyatomic gases on the shock-vortex interaction based on the second-order constitutive model of the Boltzmann-Curtiss equation, Phys. Fluids 30 (2018) 016109.

[34] S. Singh, A. Karchani, K. Sharma, R.S. Myong, Topological representation of the second-order constitutive model based on Boltzmann-Curtiss kinetic equation for diatomic and polyatomic gases, Phys. Fluids 32 (2020) 026104.

[35] T.K. Mankodi, R.S. Myong, Quasi-classical trajectory-based non-equilibrium chemical reaction models for hypersonic air flows, Phys. Fluids 31 (2019) 106102.

[36] T.K. Mankodi, R.S. Myong, Erratum: "Quasi-classical trajectory-based non-equilibrium chemical reaction models for hypersonic air flows" [Phys. Fluids 31, 106102 (2019)], Phys. Fluids 32 (2020) 019901.

[37] T. K. Mankodi, U.V. Bhandarkar, R.S. Myong, Collision cross sections and nonequilibrium viscosity coefficients of N2 and O2 based on molecular dynamics, Phys. Fluids 32 (2020) 036102.

[38] J.H. Chae, T.K. Mankodi, S.M. Choi, R.S. Myong, Combined effects of thermal non-equilibrium and chemical reactions on hypersonic air flows around an orbital reentry vehicle, Int. J. Aeronaut. Space Sci. 21 (2020) 612–626.

[39] T.K. Mankodi, R.S. Myong, Boltzmann-based second-order constitutive models of diatomic and polyatomic gases including the vibrational mode, Phys. Fluids 32 (2020) 126109.

[40] B. Sharma, R. Kumar, Estimation of bulk viscosity of dilute gases using a nonequilibrium molecular dynamics approach, Phys. Rev. E 100, 013309 (2019).

[41] S. Bhola, T.K. Sengupta, Roles of bulk viscosity on transonic shock-wave/boundary layer interaction, Phys. Fluids. 31 (2019).

[42] K. Xu, L. Tang, Nonequilibrium Bhatnagar-Gross-Krook model for nitrogen shock structure, Phys. Fluids. 16 (2004) 3824–3827.

[43] B. Evans, Nano-particle drag prediction at low Reynolds number using a direct Boltzmann–BGK solution approach, J. Comput. Phys. 352 (2019) 123–141.

[44] L. Wu, C. White, T.J. Scanlon, J.M. Reese, Y. Zhang, A kinetic model of the Boltzmann equation for non-vibrating polyatomic gases, J. Fluid Mech. 763 (2015) 24–50.

[45] C.S. Wang Chang, G.E. Uhlenbeck, Transport Phenomena in Polyatomic Gases, University of Michigan, Ann Arbor, 1951.

[46] M.H. Gorji, P. Jenny, An efficient particle Fokker-Planck algorithm for rarefied gas flows, J. Comput. Phys. 262 (2014) 325–343.

[47] V.A. Rykov, V.A. Titarev, E.M. Shakhov, Shock wave structure in a diatomic gas based on a kinetic model, Fluid Dyn. 43 (2008) 316–326.

[48] V. Kolobov, R. Arslanbekov, V. Aristov, A. Frolova, S.A. Zabelok, Unified solver for rarefied and continuum flows with adaptive mesh and algorithm refinement, , J. Comput. Phys. 223(2) (2007) 589–608.

[49] K. Xu, J. Huang, A unified gas-kinetic scheme for continuum and rarefied flows, J. Comput. Phys. 229(20) (2010) 7747–7764.

[50] L. Zhu, Z. Guo, K. Xu, Discrete unified gas kinetic scheme on unstructured meshes, Comput. Fluids 127 (2016) 211–225.

[51] A. Peng, Z. Li, J. Wu, X. Jiang, Implicit gas-kinetic unified algorithm based on multi-block docking grid for multi-body reentry flows covering all flow regimes, J. Comput. Phys. 327 (2016) 919–942.

[52] Z. J. Liu, C. Shu, S.Y. Chen, L.M. Yang, M.P. Wan, W. Liu, A novel solver for simulation of flows from continuum regime to rarefied regime at moderate Knudsen number, J. Comput. Phys. 415 (2020) 109548.

[53] B.C. Eu, Y.G. Ohr, Generalized hydrodynamics, bulk viscocity, and sound wave absorption and dispersion in dilute rigid molecular gases, Phys. Fluids. 13 (2001) 744–753.

[54] C.F. Curtiss, The classical Boltzmann equation of a gas of diatomic molecules, J. Chem. Phys. 75 (1981) 376–378.

[55] C.F. Curtiss, The classical Boltzmann equation of a molecular gas, J. Chem. Phys. 97 (1992) 1416.

[56] R.S. Myong, On the high Mach number shock structure singularity caused by overreach of Maxwellian molecules, Phys. Fluids. 26 (2014) 056102.

[57] S. Singh, R.S. Myong, Three-dimensional discontinuous Galerkin method for the second-order Boltzmann-Curtiss constitutive model in continuum-rarefied gas flows, 31st International Symposium on Rarefied Gas Dynamics: RGD31. 2132 (2019) 060013.

[58] O. Ejtehadi, R.S. Myong, A modal discontinuous Galerkin method for simulating dusty and granular gas flows in thermal non-equilibrium in the Eulerian framework, J. Comput. Phys. 411 (2020) 109410.

[59] A. Rahimi, O. Ejtehadi, K.H. Lee, R.S. Myong, Near-field plume-surface interaction and regolith erosion and dispersal during the lunar landing, Acta Astronautica 175 (2020) 308–326.

[60] A. Rana, R. Ravichandran, J. Park, R.S. Myong, Microscopic molecular dynamics characterization of the second-order non-Navier-Fourier constitutive laws in the Poiseuille gas flow, Phys. Fluids. 28 (2016) 082003.

[61] W.H. Reed, T.R. Hill, Triangular Mesh Methods for the Neutron Transport Equation, United States Department of Energy, 1973.

[62] B. Cockburn, S.Y. Lin, C.W. Shu, TVB Runge-Kutta local projection discontinuous Galerkin finite element method for conservation laws III: one-dimensional systems, J. Comput. Phys. 84 (1) (1989) 90–113.

[63] B. Cockburn, C.W. Shu, The Runge–Kutta discontinuous Galerkin method for conservation laws V: multidimensional systems, J. Comput. Phys. 141 (2) (1998) 199–224.

[64] F. Bassi, S. Rebay, A high-order accurate discontinuous finite element method for the numerical solution of the compressible Navier-Stokes equations, J. Comput. Phys. 131 (1997) 267–279.

[65] B. Cockburn, C.W. Shu, Runge-Kutta discontinuous Galerkin methods for convection-dominated problems, J. Sci. Comput. 16 (2001) 173–261.

[66] B. Cockburn, C.W. Shu, The local discontinuous Galerkin method for time-dependent convection-diffusion systems, SIAM J. Numer. Anal. 35 (1998) 2440–2463.

[67] W. Su, P. Wang, Y. Zhang, L. Wu, A high-order hybridizable discontinuous Galerkin method with fast convergence to steady-state solutions of the gas kinetic equation, J. Comput. Phys. 376 (2019) 973–991.

[68] F. Filbet, T. Xiong, A hybrid discontinuous Galerkin scheme for multi-scale kinetic equations, J. Comput. Phys. 372 (2018) 841–863.

[69] E. Madaule, M. Restelli, E. Sonnendrücker, Energy conserving discontinuous Galerkin spectral element method for the Vlasov-Poisson system, J. Comput. Phys. 279 (2014) 261–288.

[70] Y. Cheng, A.J. Christlieb, X. Zhong, Energy-conserving discontinuous Galerkin methods for the Vlasov–Maxwell system, J. Comput. Phys. 279 (2014) 145–173.

[71] S. Singh, M. Battiato, Effect of strong electric fields on material responses: The Bloch oscillation resonance in high field conductivities, Materials 13 (2020) 1070.

[72] S. Singh, M. Battiato, An explicit modal discontinuous Galerkin method for Boltzmann transport equation under electronic nonequilibrium conditions, Comput. Fluids 224 (2021) 104972.

[73] S. Singh, M. Battiato, Strongly out-of-equilibrium simulations for electron Boltzmann transport equation using modal discontinuous Galerkin approach, Int. J. Appl. Comput. Math. 6 (2020) 133.

[74] Q. Li, J. Zeng, W. Su, L. Wu, Uncertainty quantification in rarefied dynamics of molecular gas: rate effect of thermal relaxation, J. Fluid Mech. 917 (2021) A58.

[75] L. Wu, Q. Li, H. Liu, W. Ubachs, Extraction of the translational Eucken factor from light scattering by molecular gas, J. Fluid Mech. 901 (2020) A23.

[76] F.R.W. McCourt, J.J.M. Beenakker, W.E. Köhler, I. Kuščer, Nonequilibrium Phenomena in Polyatomic Gases: Volume 1 Dilute Gases, Clarendon Press, Oxford, 1990.

[77] S. Chapman, T.G. Cowling, The Mathematical Theory of Non-uniform Gases, Cambridge University Press, Cambridge, 1970.

[78] M.S. Cramer, Numerical estimates for the bulk viscosity of ideal gases, Phys. Fluids. 24 (2012) 066102.

[79] L. Onsager, Reciprocal relations in irreversible processes. I., Phys. Rev. 37 (1931) 405–426.

[80] R. E. Khayat, B. C. Eu, Generalized hydrodynamics, normal-stress effects, and velocity slips in the cylindrical Couette flow of Lennard-Jones fluids, Phys. Rev. A 39 (1989) 728.

[81] H. Xiao, R.S. Myong, Computational simulations of microscale shock-vortex interaction using a mixed discontinuous Galerkin method, Comput. Fluids. 105 (2014) 179–193.

[82] A. Karchani, Discontinuous Galerkin methods for the second-order Boltzmann-based hydrodynamic models. Ph.D. Thesis, Gyeongsang National University, South Korea (2017).

[83] S. Singh, Development of a 3D discontinuous Galerkin method for the second-order Boltzmann-Curtiss based hydrodynamic models of diatomic and polyatomic gases. Ph.D. Thesis, Gyeongsang National University, South Korea (2018).

[84] T. Chourushi, A. Rahimi, S. Singh, R.S. Myong, Computational simulation of near-continuum gas flows using the Navier-Stokes-Fourier equations with the slip and jump conditions based on a modal discontinuous Galerkin method, Adv. Aerodyn. 2 (2020) 653–664.

[85] G. Karniadakis, S. Sherwin, Spectral/hp Element Methods for Computational Fluid Dynamics, Oxford University Press, 2007.

[86] D.A. Dunavant, High degree efficient symmetrical Gaussian quadrature rules for the triangle, Int. J. Numer. Meth. Eng. 21 (1985) 1129–1148.

[87] P. Keast, Moderate-degree tetrahedral quadrature formulas, Comput. Methods Appl. Mech. Engrg. 55 (1986) 339–348.

[88] S. Gottlieb, C.W. Shu, E. Tadmor, Strong stability-preserving high-order time discretization methods, SIAM Rev. 43 (2001) 89–112.

[89] C.W. Shu, S. Osher, Efficient implementation of essentially non-oscillatory shock-capturing schemes, J. Comput. Phys. 77 (1988) 439–471.

[90] T. Liang, Q. Li, We. Ye, A physical-based gas–surface interaction model for rarefied gas flow simulation, J. Comput. Phys. 352 (2018) 105–122.

[91] J.C. Maxwell, On stresses in rarefied gases arising from inequalities of temperature, Phil. Trans. R. Soc. Lond.170 (1879) 231–256.

[92] M. Smoluchowski von Smolan, Ueber wärmeleitung in verdünnten gasen, Annalen Der Physik. 300 (1898) 101–130.

[93] J. Zhu, J. Qiu, C.W. Shu, High-order Runge-Kutta discontinuous Galerkin methods with a new type of multi-resolution WENO limiters, J. Comput. Phys. 404 (2020) 109105.

[94] H. Hajduk, D. Kuzmin, V. Aizinger, New directional vector limiters for discontinuous Galerkin methods, J. Comput. Phys. 384 (2019) 308–325.

[95] X. Zhang, C.W. Shu, On positivity-preserving high order discontinuous Galerkin schemes for compressible Euler equations on rectangular meshes J. Comput. Phys. 229 (2010) 8918–8934.

[96] X. Zhang, Y. Xia, C.W. Shu, Maximum-principle-satisfying and positivity-preserving high order discontinuous galerkin schemes for conservation laws on triangular meshes, J. Sci. Comput. 50 (2012) 29–62.

[97] J. Qiu, B.C. Khoo, C.W. Shu, A numerical study for the performance of the Runge–Kutta discontinuous Galerkin method based on different numerical fluxes, J. Comput. Phys. 212 (2006) 540–565.

[98] P. Woodward, P. Colella, The numerical simulation of two-dimensional fluid flow with strong shocks, J. Comput. Phys. 54 (1984) 115–173.

[99] H. M. Mott-Smith, The solution of the Boltzmann equation for a shock wave, Phys. Rev. 82 (1951) 885.

[100] H. Grad, The profile of a steady plane shock wave, Commun. Pure Appl. Math. 5 (1952) 257.

[101] M. Al-Ghoul, B. C. Eu, Generalized hydrodynamics and shock waves, Phys. Rev. E 56 (1997) 2981.

[102] M. Al-Ghoul, B. C. Eu, Generalized hydrodynamic theory of shock waves in rigid diatomic gases, Phys. Rev. E 64 (2001) 046303.

[103] R.S. Myong, Analytical solutions of shock structure thickness and asymmetry in Navier–Stokes/Fourier framework, AIAA J. 52 (2014) 1075.

[104] H. Alsmeyer, Density profiles in argon and nitrogen shock waves measured by the absorption of an electron beam, J. Fluid Mech. 74 (1976) 497–513.

[105] M. Camac, Argon shock structure, In Proceedings of the Fourth International Symposium on Rarefied Gas Dynamics, Adv. Appl. Mech. 1 (1965) 240.

[106] W. Garen, R. Synofzik, A. Frohn, Shock tube for generating weak shock waves, AIAA J. 12 (1974) 1132–1134.

[107] M. Linzer, D.F. Hornig, Structure of shock fronts in argon and nitrogen, Phys. Fluids. 6 (1963) 1661–1668.

[108] M. Coutanceau, R. Bouard, Experimental determination of the main features of the viscous flow in the wake of a circular cylinder in uniform translation. Part 1. Steady flow, J. Fluid Mech. 79 (1977) 231–256.

[109] T. Schwartzentruber, I. Boyd, Investigation of continuum breakdown in hypersonic flows using a hybrid DSMC–NS algorithm, 40th Thermophysics Conference, AIAA Paper (2008) 4108.

[110] K.W. Tibbs, F. Baras, A.L. Garcia, Anomalous flow profile due to the curvature effect on slip length, Phys. Rev. E 56 (1997) 2282.

[111] R.S. Myong, J.M. Reese, R.W. Barber, D.R. Emerson,Velocity slip in microscale cylindrical Couette flow: the Langmuir model, Phys. Fluids. 17 (2005) 087105.

[112] N. Dongari, R.W. Barber, D.R. Emerson, S.K. Stefanov, Y. Zhang, J.M. Reese, The effect of Knudsen layers on rarefied cylindrical Couette gas flows, Microfluid. Nanofluid. 14 (2013) 31–43.

[113] W. Su, P. Wang, H. Liu, L. Wu, Accurate and efficient computation of the Boltzmann equation for Couette flow: Influence of intermolecular potentials on Knudsen layer function and viscous slip coefficient, J. Comput. Phys. 378 (2019) 573–590.

[114] Z. Guo, B. Shi, C. Zheng, Velocity inversion of micro cylindrical Couette flow: A lattice Boltzmann study, Comput. Math. Appl. 61 (2011) 3519–3527.

[115] T. Chourushi, A. Rahimi, S. Singh, O. Ejethadi, T.K. Mankodi, R.S. Myong, Thermal and flow characteristics of nonequilibrium monatomic, diatomic, and polyatomic gases in cylindrical Couette flow based on second-order non-Navier–Fourier constitutive model, Int. J. Heat Mass Transf. 187 (2022) 122580.

[116] S. Taneda, Experimental investigation of the wake behind a sphere at low Reynolds numbers, J. Phys. Soc. Jpn. 11 (1956) 1104–1108.

[117] Z.J.W. and Y.L. Y. Sun, High-order multidomain spectral difference method for the Navier-Stokes Equations on unstructured hexahedral grids, Commun. Comput. Phys. 2 (2007) 310–333.